



ORIGINAL RESEARCH ARTICLE

# Effect of Travel Speed on the Properties of 5087 Aluminum Alloy Walls Produced by Wire and Arc Additive Manufacturing

Miroslav Sahul, Marián Pavlík, Martin Sahul, Pavel Kovačócy, and Maroš Martinkovič

Submitted: 2 May 2023 / Revised: 11 December 2023 / Accepted: 29 December 2023

An innovative Wire and Arc Additive Manufacturing combines the well-studied process of arc welding with direct energy deposition. Effect of travel speed 5.0 and 7.5 mm/s on the microstructure and mechanical properties of 5087 aluminum alloy was investigated. Five thousand eighty-three aluminum alloy was used as a substrate material and 5087 aluminum alloy was utilized as a filler material for the walls fabrication. The presence of pores reducing the strength of the overlay weld metal was detected on both overlay welds. The lower welding speed (5 mm/s) resulted in the smaller amount of porosity in comparison to higher welding speed (7.5 mm/s). Average pore area of wall No. 1 was 0.66% and wall No. 2 was 1.13%. It was found that higher welding speed affected the wall width and overlay weld bead geometry. Increase in welding speed led to a narrowing of wall width from 10.23 to 8.44 mm. The microstructure of weld metal matrix consisted of a  $\alpha$ -Al substitution solid solution. The tensile strength of parallel to welding direction removed samples exceeded the tensile strength of perpendicular removed samples. It is a result of the cohesion of the layers in the overlay welding direction compared to the non-uniformity of the layers in the perpendicular direction. Furthermore, the tensile strength was higher in the case of travel speed of 5 mm/s in comparison to that of 7.5 mm/s.

**Keywords** 5087 aluminium alloy, mechanical properties, porosity, travel speed, wire and arc additive manufacturing

## 1. Introduction

Nowadays, when it is necessary to develop more economical and flexible methods of metal components production, the wire and arc additive manufacturing technique (WAAM) is becoming more popular. Advanced WAAM method as a part of the additive manufacturing (AM) has been widely studied and applied over the last decade (Ref 1-3). It uses a metal welding wire as the feedstock (welding process side), electric arc as the heat source (AM technology side), and computer control base (automatization side). Metal products made with conventional AM technology are often porous and cannot be fully utilized. Thus, mentioned technology can offer a solution for these problems (Ref 4, 5). Furthermore, components with relatively complex geometries can be produced with high deposition rate

and fewer restrictions in material-intensive industry by using additive technologies (Ref 6, 7).

Lin et al. (Ref 8) summarized current overview included processing possibilities, automatized extension of the method, and applications focused on outputs in the WAAM field using titanium alloys. A similar review of the properties of aluminum alloys produced by the WAAM was provided by Tawfik et al. They found out that, the unsteady weld pools, wrong programming strategies and inappropriate selection of welding parameters are the main reasons of presence of defects in aluminum alloys (Ref 9-11). Aluminum alloys with its relatively low melting point are of high interest in production of structural parts (Ref 12, 13). Combination of this advantage in conjunction with WAAM allows improving cost-effective production, e.g., automotive, shipbuilding, and aerospace industries (Ref 14, 15). Hauser et al. investigated multi-material WAAM of 6060 and 5087 aluminum alloys with in-situ material analysis. The authors found that, in the case of 6060 aluminum alloy the tensile strength was limited, however the 5087 aluminum alloy with higher Mg content shows a higher hardness (Ref 16). Zhou et al. studied the influence of travel speed (TS) on mechanical properties of WAAM 2219 aluminum alloy, namely, ultimate tensile strength (UTS) and yield strength (YS). When TS increased from 150 to 350 mm/min, the UTS value increased from 216.7 to 273.5 MPa, as reported by authors. The YS presented the same trend (Ref 17). Effect of utilization of a wire with a good surface finish on the resulting porosity was evaluated in the study of Ryan et al.

Higher levels of porosity can lead to lower values of critical material properties. Thus, the micropores were considered as the predominant hydrogen traps and crack initiation and spread sites (Ref 18, 19). The authors also demonstrated that the used

Miroslav Sahul, Faculty of Mechanical Engineering, Czech Technical University in Prague, Technická 4, 166 07 Prague 6, Czech Republic; and Faculty of Materials Science and Technology in Trnava, Slovak University of Technology in Bratislava, J. Bottu 25, 917 24 Trnava, Slovakia; and Marián Pavlík, Martin Sahul, Pavel Kovačócy, and Maroš Martinkovič, Faculty of Materials Science and Technology in Trnava, Slovak University of Technology in Bratislava, J. Bottu 25, 917 24 Trnava, Slovakia. Contact e-mail: miroslav.sahul@fs.cvut.cz.

wire batch had the main effect on porosity in AA2319 alloy (Ref 19–21). Zhang et al. (Ref 22) studied microstructure and properties of ER5183 aluminum alloy parts deposited by CMT method. The authors found that the decrease in microhardness from 98.7 to 76.4 HV was accompanied with increase in grain size from 37 to 65  $\mu\text{m}$ . By using of CFD simulations, Hauser et al. suggested two main oxidation effects, namely, the oxidation anomalies such as pores, cracks, and oxidation and the surface oxidation of AW4043/AlSi5 aluminum parts during WAAM. A monitoring method based on light emission spectroscopy was used to detect oxidation anomalies. The most significant oxidation anomalies were detected in the ultraviolet wavelength ranges, from 220 to 240 nm and from 300 to 320 nm. The decreasing thickness of the surface oxide layer on aluminum parts can be mainly clarified by the existing surface oxidation before processing (Ref 23). Yongjie et al. tested the compression properties of ER2319 aluminum alloy at room temperature. The average compressive strength was 58.53 MPa, and the compression performance was stable, which determined that the diameter and angle of the struts were accurate. Mechanical properties and microstructure of Al-Zn-Mg (7xxx series) alloy samples with high processability, strength and weldability produced by WAAM technique were examined by Li et al. (Ref 24, 25). The horizontal elongation of the samples was 9.66% and average tensile strength was 324 MPa, while the vertical elongation was 8.98%, the average tensile strength was 299 MPa, and the average microhardness 112 HV (Ref 25). GTAW method (gas tungsten arc welding) is, due to the high melting temperature of tungsten (about 3420 °C) characteristic as highly efficient to produce near-net structures in comparison to other WAAM methods (Ref 26, 27). Conversely, CMT (cold metal transfer) has the advantages of stable arc, and low heat input, which results in low deformations of parts (Ref 28). Mechanical properties of 2219 aluminum alloy components fabricated with GTAW method were studied by Bai et al. (Ref 29). Similarly, microstructure and mechanical properties of 2219 aluminum alloy parts deposited with CMT process were studied by Gu et al. As observed by the authors, inter-layer cold working can eliminate creation of pores and improve the mechanical properties (Ref 30). Influence of heat treatment on microstructure and mechanical properties of 2024 aluminum alloy was documented by Qi et al. (Ref 31). In that case, the microhardness was enhanced, from 95 HV up to 138 and 146 HV. The microstructure mainly consisted of equiaxed and columnar dendrites, which morphology changed after the heat treatment.

The paper deals with the depth-in analysis of wire and arc additive manufactured (WAAMed) aluminum alloy walls by means of their chemical composition, microstructure, porosity, and mechanical properties analyses. The walls were fabricated at different travel speeds.

## 2. Materials and Methods

In this study, the 5xxx aluminum alloys were used. Thanks to the magnesium, these types of aluminum alloys possess good mechanical properties and high corrosion resistance (Ref 32). AW5083-H111 aluminum alloy was used as a substrate material and AW5087 aluminum alloy was utilized as a filler

material for the walls fabrication. The substrate plates had the dimensions of 100 × 200 × 20 mm, and the wire had a diameter of 1.2 mm. Chemical compositions of base materials are given in Tables 1 and 2 (Ref 33, 34). Mechanical properties of base plates are given in Tables 3 and 4 (Ref 35, 36). Prior to deposition, surface of substrates was cleaned by steel brush and cleaned with acetone to achieve required contact area with filler material. Fronius TPS600i welding source was used. Two planar walls with 55 and 70 WAAMed layers were made. To obtain a higher accuracy, the preheating temperature was measured with a thermocouple during the oxy-acetylene preheating. Preheating temperature was set to 350 °C.

Argon 4.6 (99.996% purity) shielding was utilized for overlay weld bead layer protection. Shielding gas flow rate was 20 l/min. The distance of the torch from the substrate was 18 mm, and torch angle was 90° (perpendicular to the substrate). Overlay welding parameters are given in Table 5. Heat input in MIG-WAAM welding was calculated according to the following equation (Ref 38):

$$Q = \frac{V \times I \times 60}{S \times 1000} \times \eta (\text{kJ/mm}) \quad (\text{Eq 1})$$

where  $V$  is welding voltage in U,  $I$  is welding current in A,  $S$  is travel speed (mm/s). The efficiency  $\eta$  of MIG process is 0.8.

The cross-sections of overlay welding walls were investigated using ZEISS LSM 700 laser scanning confocal microscope. After grinding and polishing the samples, etching by Keller's reagent (95 ml H<sub>2</sub>O/2.5 ml HNO<sub>3</sub>/1.5 ml HCl/1 ml HF) was used to reveal the microstructure. Measurements of porosity on the cross-sections after polishing were made with the ImageJ software to use the appropriate representation of the porosity content in various areas of the walls. Each measured value is the arithmetic mean of five measurements. Experiments were carried out with JEOL JSM 7600 F high-resolution scanning electron microscope fitted with Oxford Instruments X-Max 50 mm<sup>2</sup> EDS Si(Li) detector to characterize the microstructure and elemental composition of the individual layers of the component. Tinus Olsen 300 ST universal testing machine was used for measurements of tensile strength of walls. Tensile strength test was carried out at room temperature in accordance with STN EN ISO 6892-1:2019 to obtain stress–strain curves. The temperature of each layer was measured by K-type thermocouple immediately after deposition of each layer in the center of length of weld bead by contacting the thermocouple tip with the surface of deposited weld bead. Waiting time between deposition of each layer was 120 s. 3D schematic diagram of WAAM workplace is shown in Fig. 1(a) and schematic overview of overlay welding of aluminum alloy is given in Fig. 1(a). Alternating directions strategy direction was used.

**Table 1 Chemical composition of 5083 aluminum alloy (in wt.%)**

Mg	Mn	Zn	Cr	Si	Fe	Cu	Ti	Al
4.5	1.0	0.25	0.25	0.4	0.4	0.1	0.15	Balance

**Table 2 Chemical composition of 5087 aluminum alloy (in wt.%)**

Mg	Mn	Zn	Cr	Si	Fe	Cu	Ti	Zr	Al
5.2	1.1	0.25	0.25	0.25	0.4	0.05	0.15	0.2	Balance

**Table 3 Mechanical properties of 5083 aluminum alloy (Ref 37)**

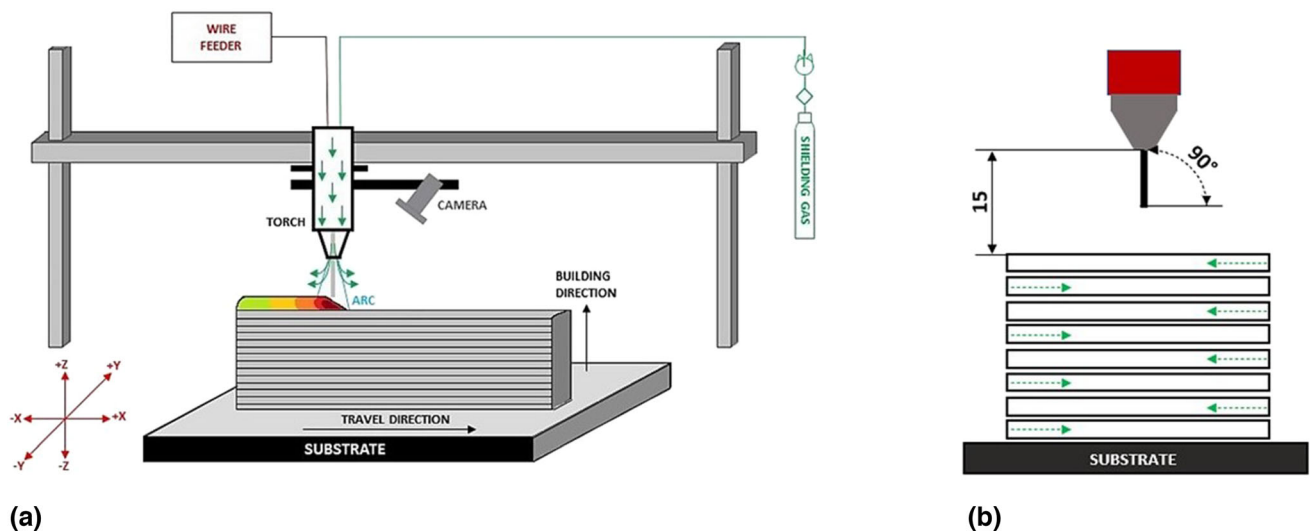
Yield strength Rp0.2, MPa	Tensile strength Rm, MPa	Ductility, %
125	275	16

**Table 4 Mechanical properties of 5087 aluminum alloy (Ref 37)**

Yield strength Rp0.2, MPa	Tensile strength Rm, MPa	Ductility, %
130	280	18

**Table 5 Overlay welding parameters**

Wall no.	Welding current, A	Welding voltage, V	Wire feed speed, m/min	Travel speed, mm/s	Pulse/ dynamics correction	Preheating temperature, °C	Heat input, J/mm
1	85	13.9	5	5.0	0.2	350	189
2	85	13.9	5	7.5	0.2	350	126

**Fig. 1** (a) Schematic diagram of WAAM system, (b) scheme of the overlay welding strategy

### 3. Results and Discussion

#### 3.1 Visual Inspection

Geometry, surface, integrity, and defects of the walls were investigated. Visual inspection of the wall No. 1 (Fig. 2a) revealed more uneven formation of the wall geometry. Higher

corrugation along the length of the wall No. 1 was found. In this case, the travel speed was set to 5 mm/s. There was non-constant time between the overlaying process of the individual layers. No cracks or pores were observed. In some places of the wall No. 1 weld spatter was documented. The width of the weld deposit was non-uniform. The average wall width was 10.2 mm. The height in the center of the wall No. 1 was



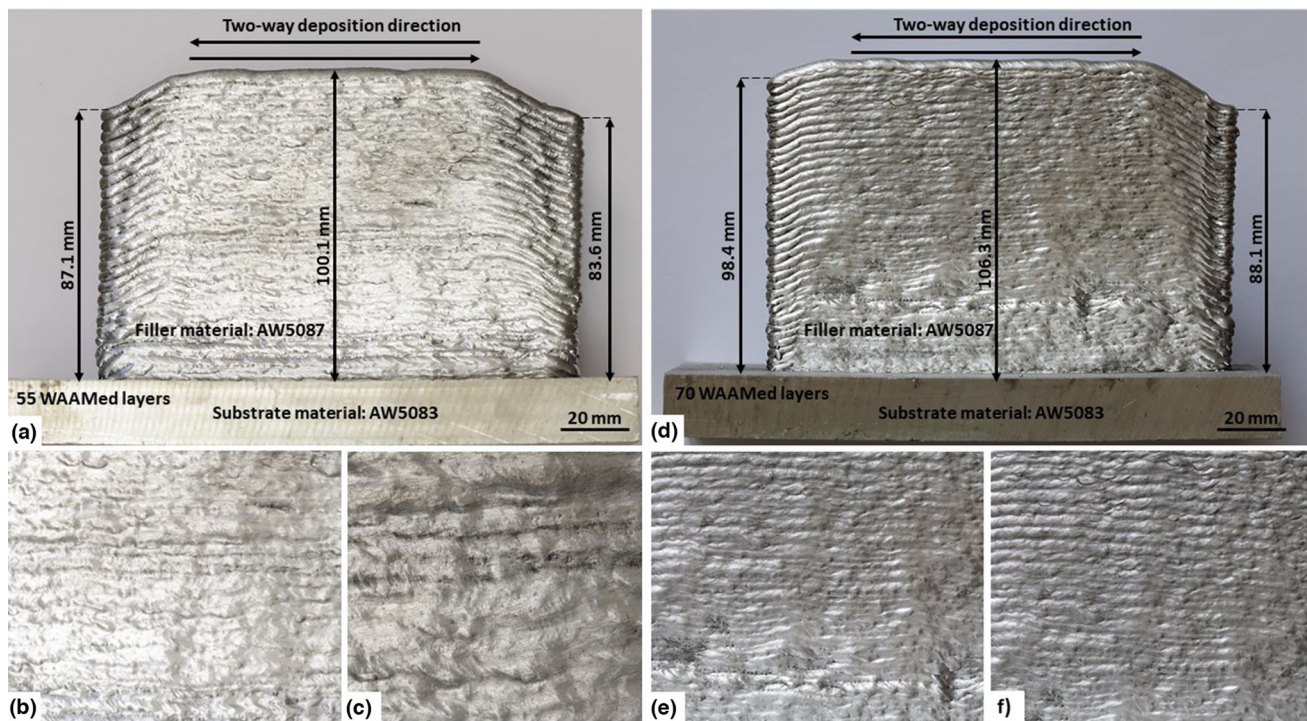


**Fig. 2** (a) Visual inspection of planar wall No. 1 (b,c) No. 1 in more detail and (d) planar wall No. 2 (e,f) No. 2 in more detail

100.1 mm. The height of the start and end of the wall was lower than the central part. The difference in height was about 15 mm as can be seen in Fig. 2(a). Figure 2(b), and (c) shows part of the planar wall No. 1 in more detail. During the fabrication of the planar wall No. 2, the travel speed increased to 7.5 mm/s. In the case of planar wall No. 2, the heat input decreased from 189 to 126 J/mm. More even formation of the wall geometry at the surface was documented. Less corrugation along the length of the wall No. 2 was identified. Significant decrease in the wall height 18.2 mm in comparison to wall height was observed. Causes of height drop of the end needs to be further examined. Weld spatter was observed in some places as well. No cracks or pores were identified. Due to the heat input, the substrate deformed during the formation of the wall No. 2 as can be seen in Fig. 2(d). Figure 2(e), and (f) shows part of the planar wall No. 2 in more detail. The layer geometry relates to the conditions of heat dissipation from various layers. The bead geometry in one welding pass is not uniform, especially at its beginnings and ends. At the start of the bead (the arc-igniting phase), the profile is wide and high, while the end of the bead is small and sloping where the arc ends (Fig. 2a, and d).

The MIG-WAAM pulse mode was selected for the fabrication of planar walls. The pulsed electric arc is made up of a low-power base current phase and a high-power pulsed current phase without short circuits material transfer. Optimal melting pool control reduces heat input, spatter, deformations, and stresses. Contamination of a welding nozzle by spatters can reduce shielding gas flow, which may then become turbulent.

The stability of the welding process depending on the composition of used shielding gas was investigated by Suban and Tušek (Ref 39). Figure 3 shows the dependence of welding current on time in different phases of single-layer overlay welding. The dependence of welding current on time at the beginning of the overlay welding is given in Fig. 3(a). The course of the welding current as a function of time from the start of welding to 0.013 seconds is given. The beginning of the overlay welding process is characterized by a higher current of around 600-650 A. Subsequently, there is a gradual current decrease, then the process settles down. Figure 3(b) shows the dependence of welding current on time during the process of overlay welding at period from 14.135 to 14.156 seconds, i.e., time interval 21 ms. Based on the contour created by the selected points the MIG pulse process appeared stable. The welding current fluctuated uniformly with the welding time as can be seen. The steady period of the pulse welding current is around 325 A. The base current was about 50 A. No significant deviations were monitored. Dependence of welding current on time at the end of the process is given in Fig. 3(c). The graph demonstrates the waveform in period from 28.6 seconds to the end of the overlay welding.

### 3.2 Analysis of Overlay Weld Cross-Sections

Individual weld beads were deposited at various travel speeds. The influence of the travel speed on the geometry of single beads is evaluated (Fig. 4). The travel speeds ranged from 3.5 to 13 mm/s. The application of travel speed of

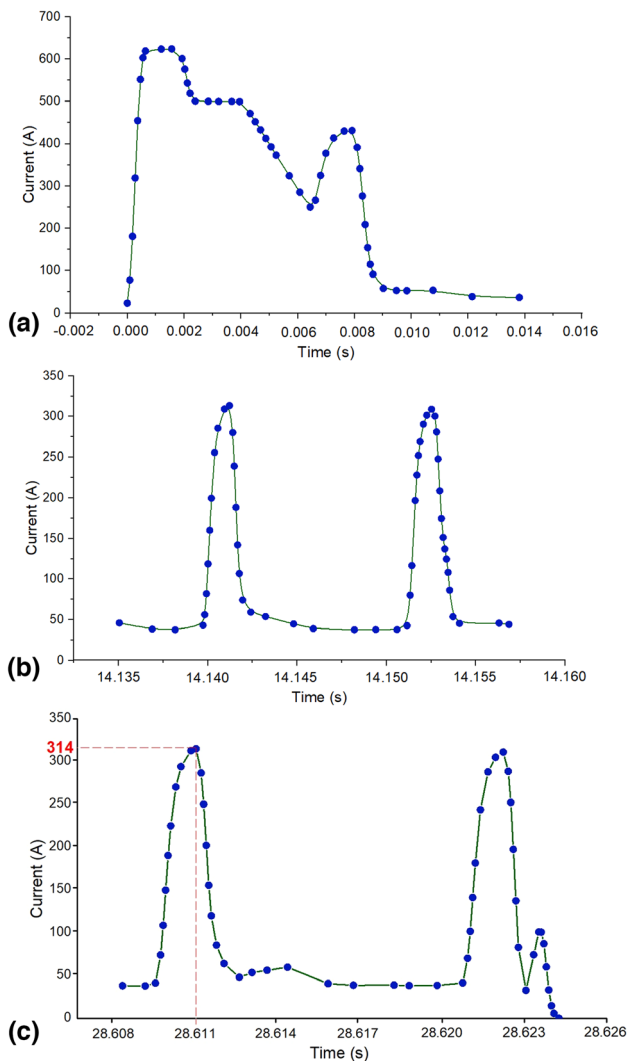


**Fig. 3** Dependence of welding current on time (a) at the beginning of the process, (b) during the process and (c) at the end of the process

3.5 mm/s resulted in the bead width of 15.3 mm. In the remaining weld beads, the higher the travel speed the narrower the deposited weld bead (Fig. 5a). The widest weld bead was observed at the travel speed of 5 mm/s reaching the value of 19.7 mm. As it was expected, the narrowest weld bead was observed at the travel speed of 13 mm/s, i.e., only about 13.4 mm. Similar trend was observed also in the case of weld bead height (Fig. 5a). Except of 3.5 mm/s, the higher the travel speed used the smaller the height of weld bead. The highest weld bead was observed when 5 mm/s travel speed was used and the lowest one in the case of application of 13 mm/s travel speed.

Furthermore, the depth of penetration of the deposited weld bead and penetration area as well, were analyzed (Fig. 5b). Increase in travel speed from 3.5 to 7.5 mm/s resulted in the increase in penetration depth from 2.6 to 4.4 mm. Further increase of travel speed to 10 and 13 mm/s resulted in the

decrease in the depth of penetration. Similar situation was recorded in the case of penetration area. The increase in travel speed from 7.5 to 10 mm/s gave the drop of penetration area from 25.8 to 9 mm<sup>2</sup>.

The presence of internal defects, the depth, and the width of the overlay welds were examined by means of cross-sectional study. Penetration depths of first layers were investigated as well. Each value represents the arithmetic mean of the five measurements. The macrostructure of the wall No. 1 is shown in Fig. 6(a). Figure 6(c) shows the substrate—first layer connection of the wall No. 1. The first layer penetration depth is 3.1 mm. No angular deformations of the base metal were observed. Cross-section of the planar wall No. 1 is characterized by visible lateral z-axis misalignment. The sufficient layer connection of the next overlay weld layer was discovered. The width of the wall No. 1 has not been narrowed or widened. No cracks are visible in Fig. 6(c). Due to the supposed presence of hydrogen, the presence of pores was observed. In the case of the wall No. 2 (Fig. 6b), travel speed increased from 5 to 7.5 mm/s. Other parameters were constant. It resulted in a reduction in heat input during the process of wall No. 2 production. In the first third of cross-section slight misalignment from z-axis was identified (Fig. 6b). However, the wall geometry has not been changed. Furthermore, the presence of pores was detected (Fig. 6d). Lower heat input affected the geometry of the overlay weld and resulted in the first layer penetration depth up to 3.63 mm.

The temperature in the middle of each layer was measured by thermocouple during the process. Inter-operational time between deposition of each layer was 120 s. With the increase of the wall height, i.e., the number of deposited layers, the lower temperature was detected. Layer temperature interval for wall No. 2 ranged from 76 to 200 °C (Fig. 7). Due to the applied preheating temperature of 350 °C, the temperature of the first layer was the highest up to 200 °C. The heat input and preheating temperature had a great impact on the geometry of the welds and the connection of the first layer to the base metal. The highest temperature measured after deposition of the first weld bead is affected also by the mentioned preheat of the base material. Preheat helped to accumulate the heat and slow down the cooling rate. The second layer was deposited after 120 s waiting time after deposition of the first bead. During this period, cooling in terms of heat dissipation toward thick base plate occurred. The temperature immediately after deposition of the second layer was 110 °C. Again, the waiting time was set to 120 s and the measured temperature at the center of the third layer immediately after its deposition was 115 °C. The decrease of the bead temperature is associated with better heat dissipation toward the lower parts of deposited wall. After the deposition of 26th layer, the measured temperature directly after deposition of layer dropped below 90 °C. This is attributed with the fact, that the heat was more effectively conducted along the height wall toward lower parts of the deposits. A narrower wall width was observed when the heat input decreased. Furthermore, the height of the wall was lower with a lower heat input.

The dependence of layer width on layer number is shown in Fig. 8. The width of the widest layer of wall No. 1 was



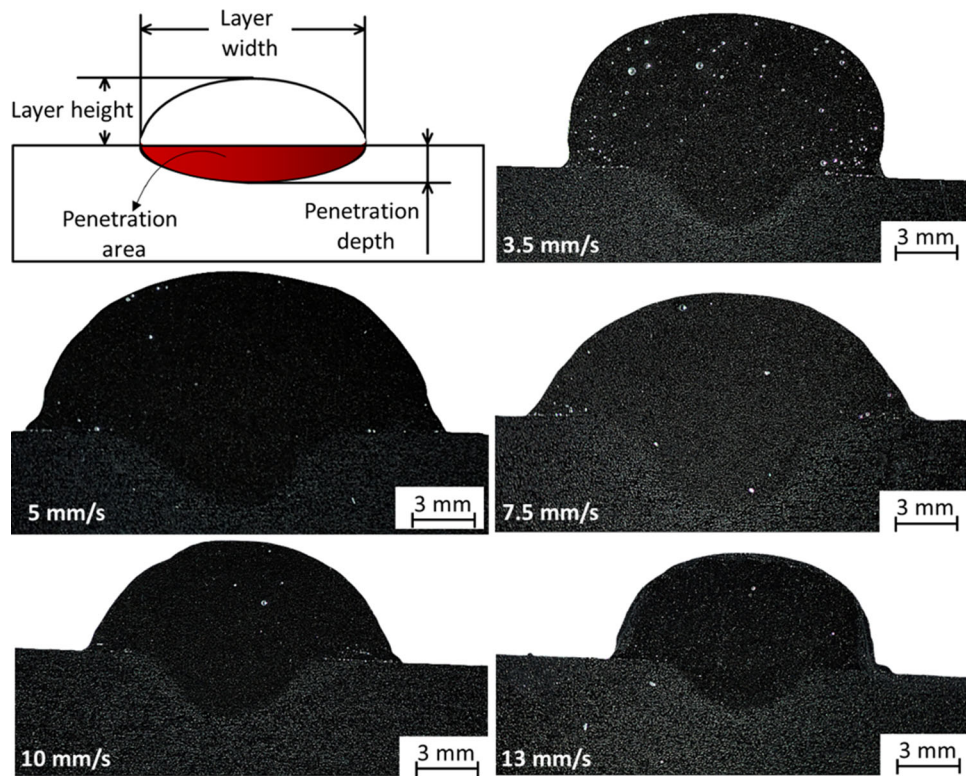


**Fig. 4** The cross-section of weld bead schematically sketched with measured dimensions and deposited at travel speeds of 3.5, 5, 7.5, 10 and 13 mm/s

11.05 mm, and vice versa the narrowest width was 9.4 mm. The average width of the layers of wall No. 1 was 10.23 mm. The width of the widest layer of wall No. 2 was 9.33 mm, and the narrowest width was 7.75 mm. The average width of the layers of wall No. 2 was 8.44 mm. It is obvious, that the welding speed was a significant parameter for the layer width value of the overlay welded beads (Fig. 8).

The experimental results (Fig. 9) showed that the height of the wall No. 1 fabricated with travel speed of 5 mm/s is almost the same as the wall No. 2 produced with travel speed of 7.5 mm/s. Compared to the wall No. 2 with 70 layers, the wall No. 1 only consisted of 55 layers. The height of both walls increased linearly with number of layers. Total wall height of No. 1 sample was 105.83 mm and total wall height of No. 2 was 105.12 mm. The height of 55 layers of wall No. 2 was about 22.51 mm lower than the height of 55 layers of wall No. 1. It is obvious, that the walls height control can be realized by changing the travel speed, which has a substantial effect on it.

### 3.3 Microscopic Analysis

The changes of individual overlay weld areas microstructures were investigated in detail. The base material was delivered in annealed and slightly hardened condition. The microstructure of 5083 aluminum alloy (base metal) possessed a polyhedral character (Fig. 10a). Because of application of preheating the surface to 350 °C the slight deformation disappeared. The microstructure consists of a  $\alpha$ -Al substitution

solid solution. First overlay weld layer (FOWL)—heat-affected zone (HAZ)—base material transition of wall No. 2 (travel speed of 7.5 mm/s) is documented in Fig. 10(b). The microstructure of weld metal consists also of  $\alpha$ -Al solid solution according to binary phase diagram Al-Mg.

The equilibrium binary phase diagram of Al-Mg (Fig. 11) indicates two solid solutions, i.e., Al(Mg) and Mg(Al) and three other different phases at room temperature. If an equal content of both elements are presented in the overlay weld metal, it leads to the formation of mixture of  $\text{Al}_3\text{Mg}_2$  ( $\beta$ ) and  $\text{Al}_{12}\text{Mg}_{17}$  ( $\gamma$ ) phases, which reflected in the mechanical properties can cause low overlay weld quality (Ref 39, 40).

The segregation of the  $\text{Al}_3\text{Mg}_2$  phase in the interdendritic areas can be assumed based on binary phase diagram of Al-Mg (Fig. 12a). The microstructure of deposited layers of wall No. 1, namely layer 1 designated as inner-layer, inter-layer consisting of second layer HAZ and next inner-layer being layer 2 is given in Fig. 12(a). Columnar dendritic zone was observed in the inner-layers 1 and 2. Columnar grains grew perpendicular to HAZ grains (Fig. 12b). The microstructure of deposited layers of wall No. 2, namely layer 2 designated as inner-layer, inter-layer consisting of third layer HAZ and next inner-layer being layer 3 is given in Fig. 12(c). The higher welding speed resulted in this case to formation of equi-axed dendrite microstructure given in Fig. 12(d). On the other hand, the presence of pores reducing the strength of the overlay weld metal was detected on both overlay welds.

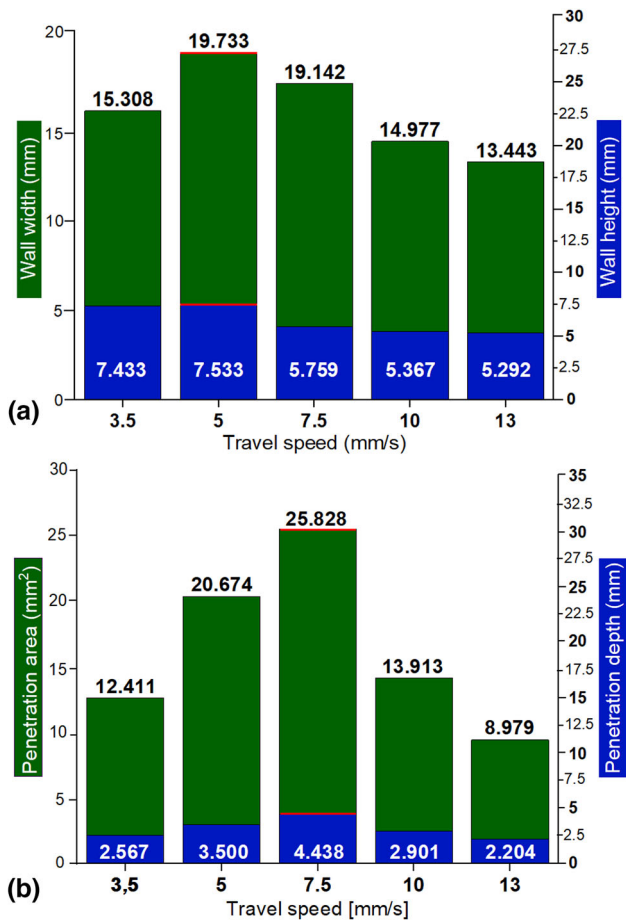


**Fig. 5** The influence of travel speed on the (a) bead width and height, and (b) penetration area and depth

### 3.4 Ultimate Tensile Strength Test

The presence or the absence of surface and internal defects, as well as the temperature of the test environmental and material may be crucial factors for the correctness of ultimate tensile strength (UTS) testing results. Based on data provided by the manufacturer, the 5087 aluminum alloy weld consumable is expected to give typical tensile strength of 280 MPa. Figure 13 shows ductility calculations for wall No. 1 and wall No. 2, which were measured from the extension of the entire test specimen  $L_0 = 40$  mm. The test specimens were cut perpendicularly and parallel to the direction of overlay welding. In Fig. 13, the test specimens cut in the parallel direction achieved a higher ductility compared to those cut in the perpendicular direction. For the wall No. 1 in the perpendicular direction, it was 0.33% less in comparison with the wall No. 2. In parallel direction, the wall No. 2 possessed higher ductility by 2.12% compared to the wall No. 1. For ductile materials, contraction (Z) depends on the material type and the test conditions, and its value increases faster than the ductility due to the formation of the neck, i.e.,  $A < Z$  (Ref 41). A higher welding speed (7.5 mm/s) caused higher ductility in both

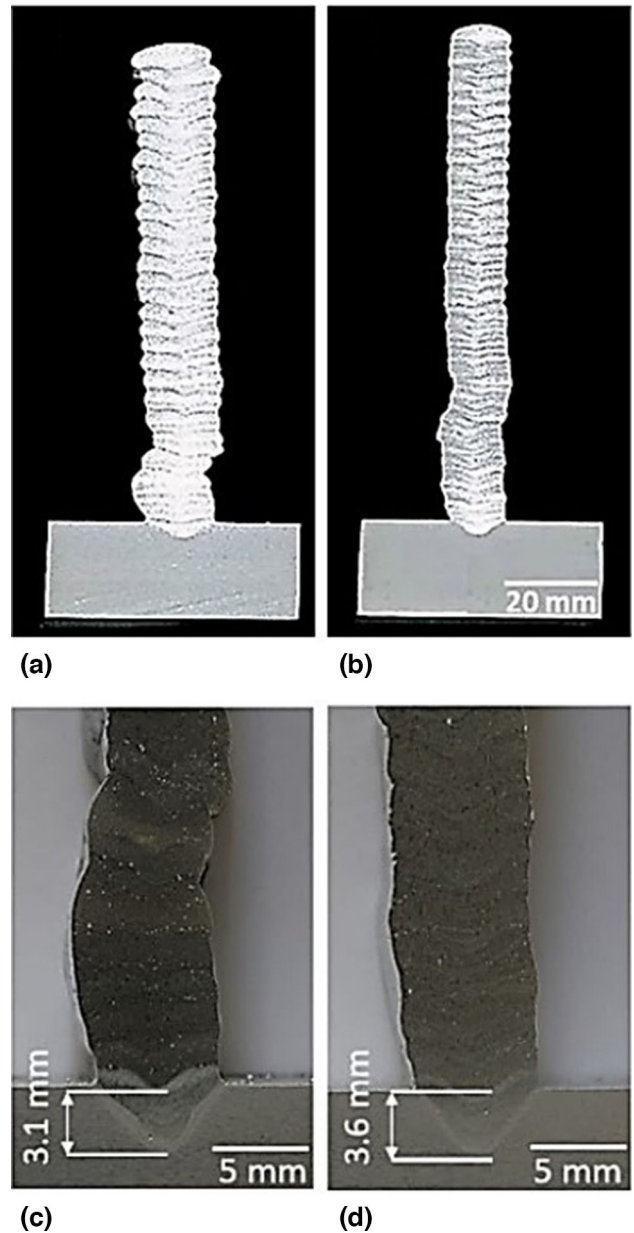


**Fig. 6** Cross-section of (a) wall No. 1 (b) wall No. 2, penetration depth of the first layer for (c) wall No. 1 (d) wall No. 2

perpendicular and parallel directions compared to a lower welding speed (5 mm/s). The average value of the contraction of the wall No. 1 parallel specimen was 30.4% and for the perpendicular specimen 29.31%. For the parallel and perpendicular specimens of the wall No. 2 specimen, the contraction was 37.63 and 31.17%, respectively. The contraction Z was obtained by the formula:

$$Z = \frac{S_0 - S_u}{S_0} \times 100(\%) \quad (\text{Eq 2})$$

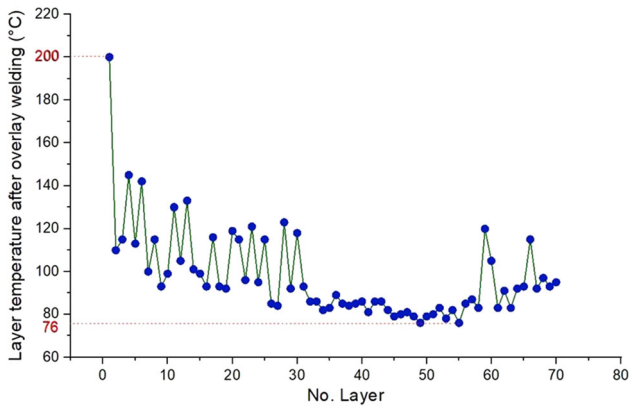


**Fig. 7** Dependence of layer temperature on number of layer of the wall No. 2

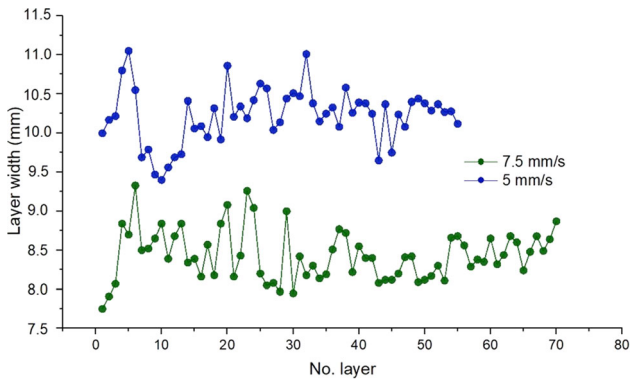


**Fig. 8** Dependence of layer width on number of layer of the wall No. 1 (5 mm/s) and wall No. 2 (7.5 mm/s)

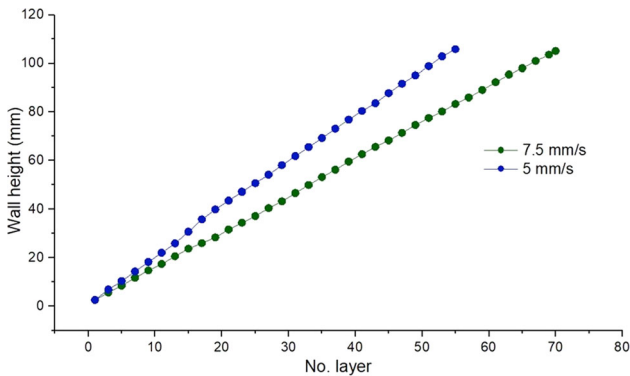


**Fig. 9** Dependence of wall height on No. layer of the wall No. 1 (5 mm/s) and wall No. 2 (7.5 mm/s)

where  $S_0$  is the area of the neck before the UTS and  $S_u$  equals to the area of the neck after the UTS.

It can be deduced that the mechanical properties (contraction) decrease with the increasing value of the content of impurities and other admixture in the metal, which cause the formation of voids in the neck during plastic deformation. It also applies that the contraction value decreases with increasing strength (Ref 42).

Furthermore, it is possible to see in Fig. 14 that the higher tensile strength was measured in the samples removed in the direction of welding. Tensile strength of sample removed in the direction perpendicular to welding direction was 261 MPa (wall No. 1). The tensile strength of sample removed in the direction parallel to welding was to 276 MPa (the wall No. 1). Similar trend was recorded also in the case of wall No. 2. Tensile strength of parallel sample was 262 MPa and that of perpendicularly oriented sample was 246 MPa (the wall No. 2). Application of a lower welding speed resulted in an increase in tensile strength by 6% in average. The dashed line at 280 MPa represents the tensile strength of the pure weld metal.

### 3.5 Porosity Level Measurement

Porosity, as one of the adverse and most occurring factors, is a key issue and a major challenge in WAAM of aluminum alloys. Porosity is caused by very different solubility values of hydrogen, either in liquid or solid state. As illustrated by Boeira et al. the solubility of hydrogen is 0.65 and 0.034 ml/100 g for solid and liquid pure aluminum, respectively (Ref 43). Porosity control is considered as one of the areas potentially suitable for new developments in the WAAM method (Ref 44). Figure 15(a), (b), and (c) shows the cross-sections of the wall at different locations, namely at the bottom of the wall, at the central part of the wall and on the top of the wall deposited at the travel speed of 5 mm/s. Spherical porosity was observed at mentioned locations. The porosity measured at the bottom of the wall produced with the travel speed of 5 mm/s reached almost 0.8%. In the central part of the wall, the porosity of 0.58% was measured and at the top of the wall, the porosity of 0.6% was attained. The mean porosity of the wall is 0.66%.

Due to the higher welding speed, the pores do not have time to diffuse out of the molten pool. As a result, a higher degree of porosity occurred after solidification of wall No. 2 leading to lower mechanical properties.

Figure 16(a), (b), and (c) shows the cross-sections of bottom of the wall, central part of the wall and top of the wall deposited at the travel speed of 7.5 mm/s. Larger amount of spherical porosity was observed at mentioned locations in comparison to wall deposited with the travel speed of 5 mm/s. The porosity measured at the bottom of the wall produced with the travel speed of 7.5 mm/s reached 1.25%. In the central part of the wall, the porosity of about 1% was measured and at the top of the wall, the porosity of about 1.1% was attained. The mean porosity of the wall is 1.13%.

Porosity below 1% does not affect mechanical properties of 2319 WAAM walls, whereas the as-built microstructure and applied heat treatment highly influence the properties obtained, as reported by Arana et al. (Ref 45). The lower welding speed (5 mm/s) in our study resulted in the smaller amount of porosity in comparison to higher welding speed (7.5 mm/s).

Distribution of pores in wall No. 1 (TS 5 mm/s) according to the pore diameter is given in Fig. 17(a), and (b). Based on the measured results, it can be stated that 72% of all detected pores have diameter up to 100  $\mu\text{m}$  (Fig. 17a). The share of pores with diameter larger than 100 up to 200  $\mu\text{m}$  was about 10%. In the case of wall No. 2 produced at the travel speed of 7.5 mm/s, the share of the pores with the diameters up to 100  $\mu\text{m}$  was almost 77%. The content of pores with the diameter greater than 100 up to 200  $\mu\text{m}$  was 4.5% (Fig. 17b).



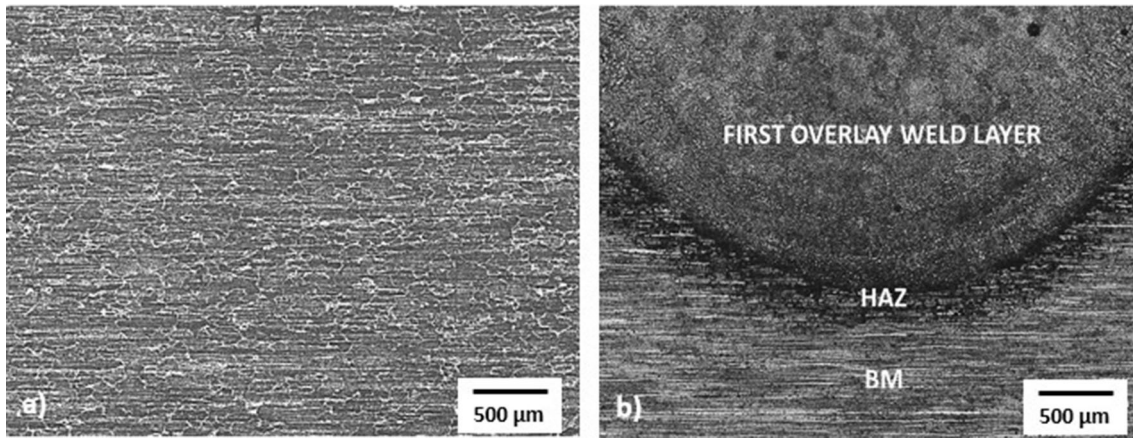


Fig. 10 Microscopic analysis of (a) BM and (b) FOWL–HAZ–BM interface

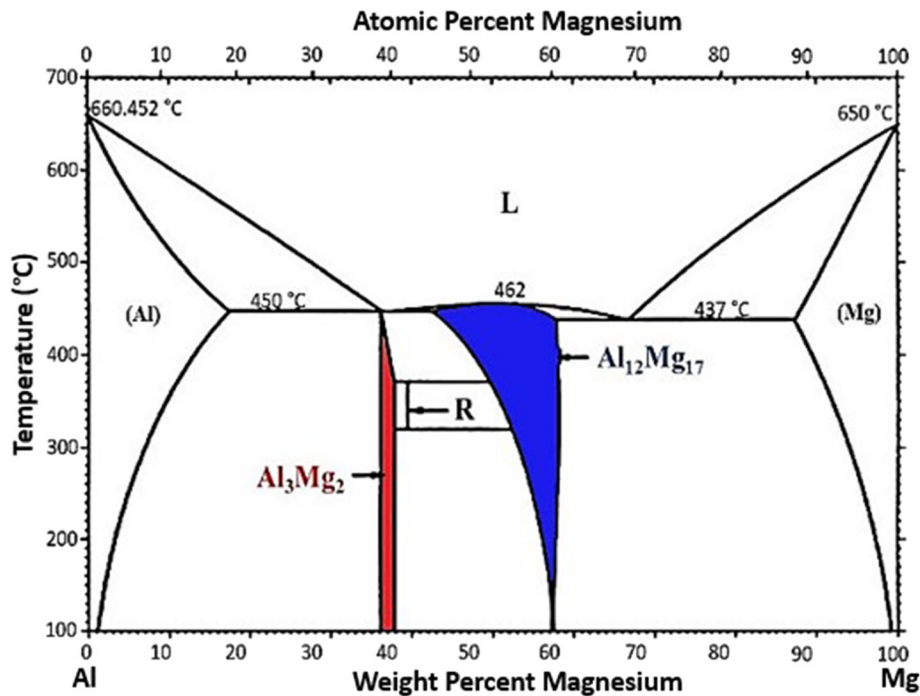


Fig. 11 Binary phase diagram of Al-Mg

### 3.6 EDS Analysis

Microstructure and chemical composition of the overlay weld of wall No. 1 at individual places was documented by scanning electron microscopy (SEM). EDS analysis (Fig. 18) was performed for quantification of chemical elements presented in the overlay welds and their distribution at different sites (wall No. 1).

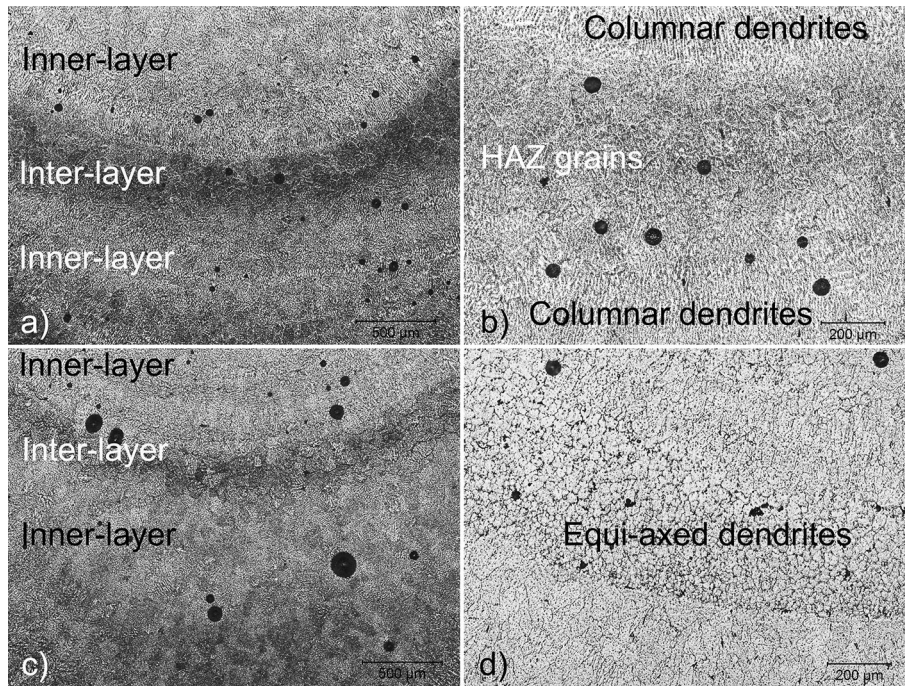
No chromium and a reduced manganese value in Spectrum 1 were observed. 0.10 at.% chromium was detected only in Spectrum 3. In brighter sites (Spectra 1, 3 and 6), lower magnesium values (4.39, 4.53 and 3.98 at.%) were indicated. Circular darker sites were characterized by higher magnesium content. Black sites (Spectra 7, 8 and 9) indicated inter-dendritic region caused by faster subcooling. The highest level of magnesium (6.30 at.%) in Spectrum 7 was found. Chemical composition results of wall No. 1 in local sites are shown in

Table 6. In addition to reduced levels of chromium, manganese, and zirconium large differences of chemical composition between manufactured components and filler material were not confirmed by EDS point analysis.

Elemental maps of Mg, Mn, Al with color definition can be utilized to differentiate chemical elements of overlay weld metal which is apparent in Fig. 19. The chemical element mapping provided further evidence that the increased amount of manganese in individual places resulted in the absence of magnesium and aluminum.

### 3.7 Fracture Morphology

SEM images of fractured surfaces of different processed samples after tensile testing showed various dimples sizes. In addition, more fine pores were found. It may be caused by the effects of Mg volatilization, porosity formation or alloying. In



**Fig. 12** Microstructure of deposited layers of (a) wall No. 1, (b) interface between columnar dendritic zone and HAZ (No. 1) and Microstructure of deposited layers of (c) wall No. 2, (d) equi-axed dendrite zone (No. 2)

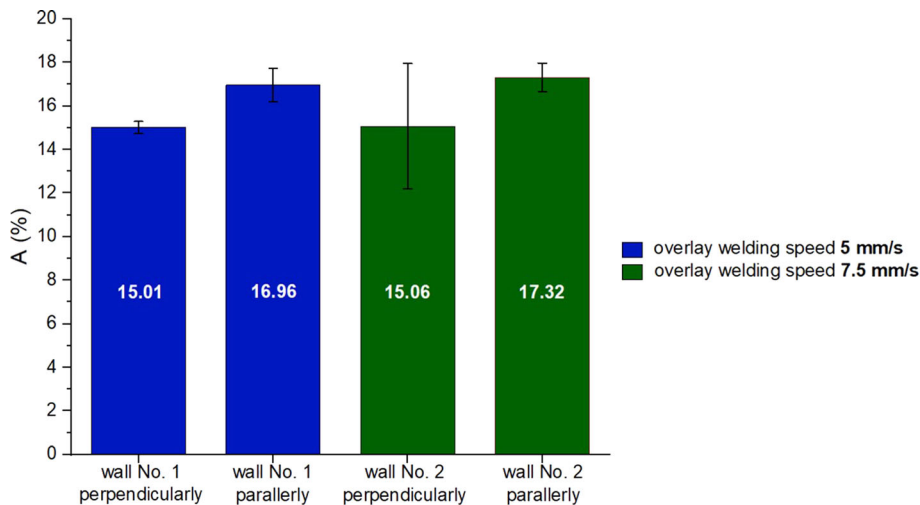


**Fig. 13** Influence of overlay welding direction and travel speed on ductility

addition, the fracture surface of the applied alloy in Fig. 20(a), (c) and 21(a), (c) shows coarser and cracked second phase particles embedded in the dimples, that can reduce the tensile strength. This is because in the case of ductile materials, the crack is formed by the coalescence of micropores that can be formed as a result of cracking the second phase particles. The cracks may initiate from micropores and then expand to macrocracks. It can be found that test samples yield with a ductile failure appearance, showing predominant presence of

dimples with tearing morphology in the deposited metal (Ref 34).

Most induced pores in aluminum weld metal are formed by undissolved hydrogen, which is due to a large solubility difference between the liquid and solid phases. Most of the excess hydrogen in aluminum applied by WAAM exists as molecular hydrogen in pores. Hydrogen elements mainly come from the surface of the aluminum substrate, welding wire, and protective gas atmosphere (Ref 21). Majority of the residual



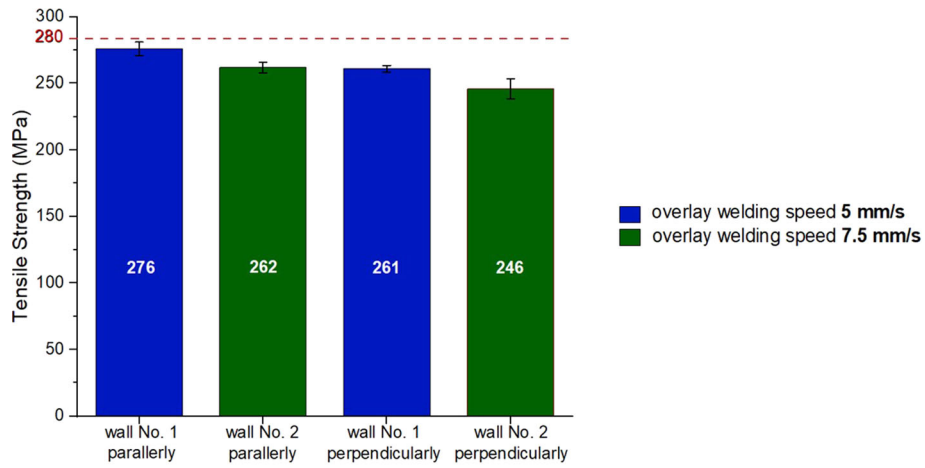


Fig. 14 Influence of travel speed and welding direction on tensile strength

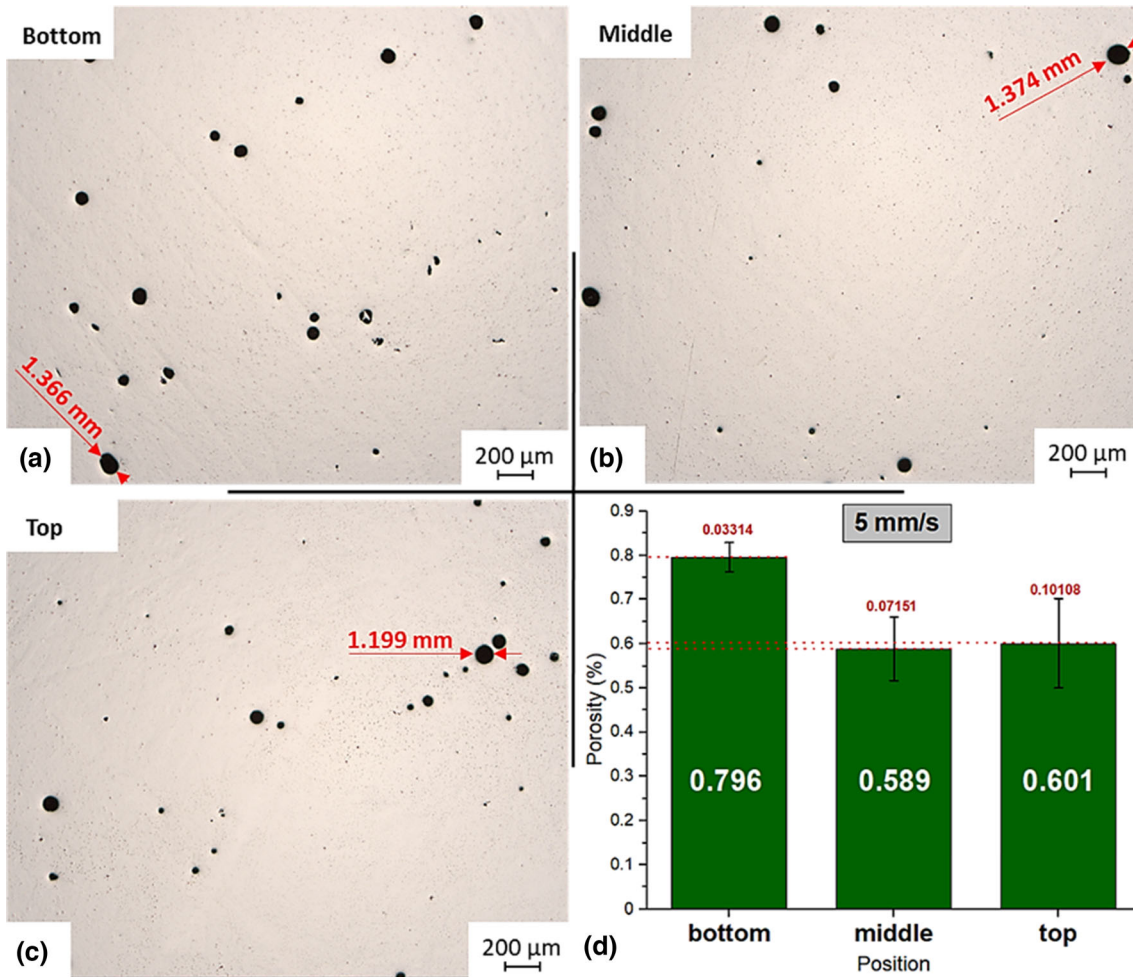


Fig. 15 Measurement of porosity on the cross-sections of (a) bottom, (b) middle, and (c) top part of deposited wall, (d) porosity measurements results (travel speed 5 mm/s)

hydrogen atoms are located at pores interior regions, that are depicted as a darker area (Fig. 22). Brighter areas are characterized by lower oxygen content and higher aluminum content (up to 90.89 at.%), based on the lateral distribution of elements from the imaged area named as Spectrum 2 (Table 7).

#### 4. Discussion

The influence of the orientation of deposition direction (perpendicular and parallel direction) of test specimens for tensile testing is evident. Also, lower travel speed (5 mm/s)



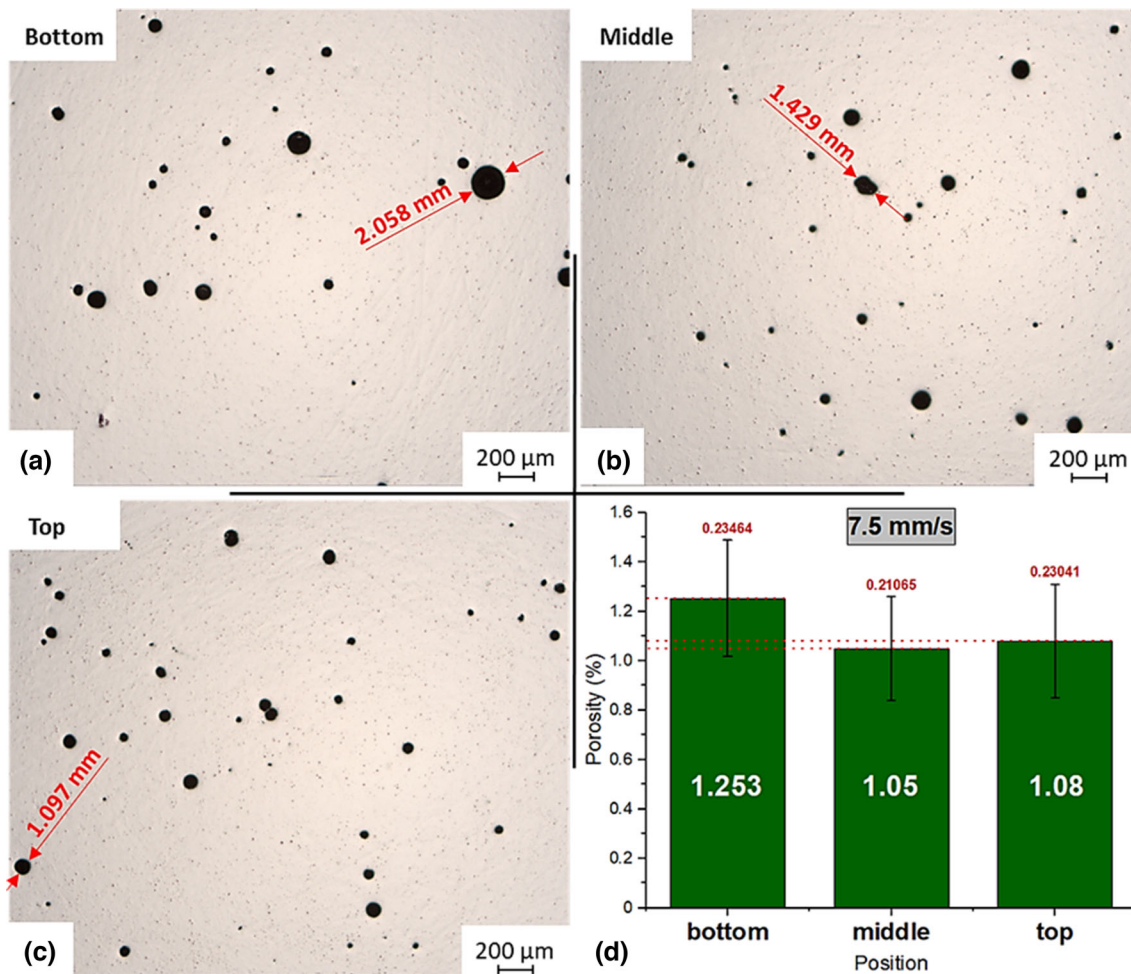


**Fig. 16** Measurement of porosity on the cross-sections of (a) bottom, (b) middle, and (c) top part of deposited wall, (d) porosity measurements results (travel speed 7.5 mm/s)

caused an increase in tensile strength in comparison with higher travel speed (7.5 mm/s), by approximately 5.5%. Sinha et al. evaluated the effect of travel speed on the mechanical properties of 2319 aluminum alloy. Deposition speeds of 2.5, 5.8 and 7.5 mm/s were analyzed. With an increase in processing speed from 2.5 to 5.8 mm/min, the UTS recorded an increment from 216.7 to 273.5 MPa. However, it declined to 259.6 MPa for the deposits made at deposition speed of 7.5 mm/s. Too high value of the travel speed can lead to non-uniform defective deposit with deteriorated mechanical properties. The microstructural properties of 2319 aluminum alloy were characteristic up to a travel speed of 5.8 mm/s by finer grains. Subsequently, increasing the speed resulted in a coarsening of the structure. (Ref 46). Welding current was set to 85 A. Deposition speed of overlay welding (5 mm/s) fabricated perpendicularly reached a magnesium content of up to 5.53 at.%. Which is up to 6.87% more compared to the deposition speed of 7.5 mm/s (perpendicular), when reached a value of 5.15 at.%. In the parallel direction, a decrease of Mg by 2.83% was detected (Fig. 23c). At an increased travel speed (up to 7.5 mm/s) and a current set at a mutually dependent

value, there was a slight decrease in the magnesium content both in the parallel and in the perpendicular direction, by approximately 4.82%. It must be considered that 70% of the heat generated during MIG process is on the electrode (which forms the main component of the overlay welding) and thus there is a possibility for higher Mg loss rate (Ref 47). This directly affected the deterioration of mechanical properties. Ren et al. refer to the reduction of Mg, which affected the mechanical properties. Increasing the Mg content will reduce the nucleation probability of pores and hinder their growth, which is the reason of decrease in the number and size of pores while the Mg content increases from 5 to 6% that correlates with Fig. 14 (Ref 48). Mg evaporation occurs especially while metal transferred the area where the temperature was higher than the boiling point Mg, namely 1107 °C, what directly affected the deterioration of mechanical properties.

The influence of welding current and deposition speed on Mg loss rate in WAAM processed aluminum alloy was investigated by Yuan et al. Authors found that the Mg loss rate (Fig. 23a, and b) that causes substitutional hardening of the alloys and improves their strain hardening ability (magnesium

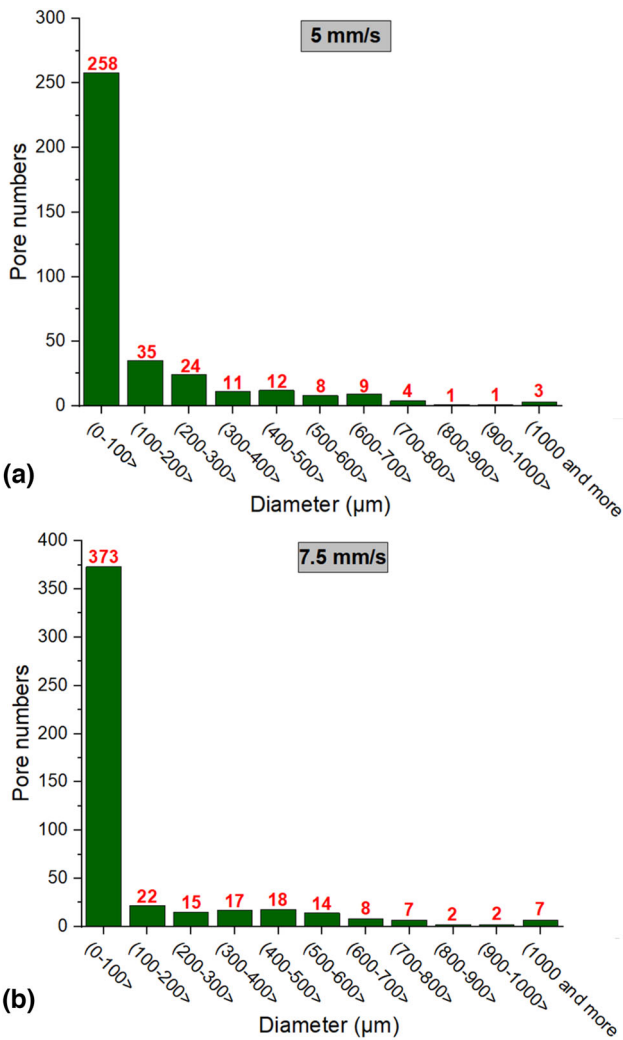


Fig. 17 Distribution of pores in wall deposited at travel speed of (a) 5 mm/s, (b) 7.5 mm/s

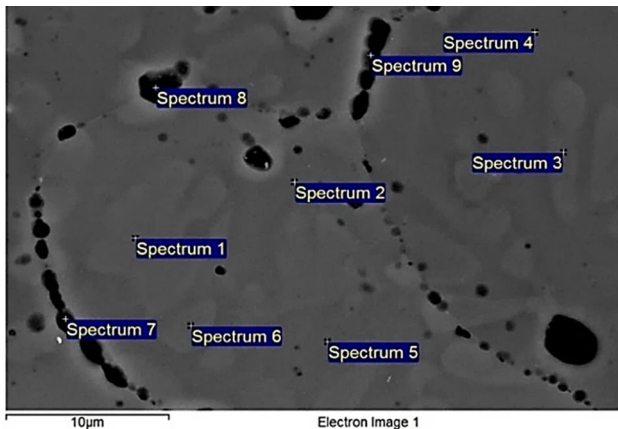


Fig. 18 EDS point analysis at local sites in the overlay weld metal of wall No. 1

Table 6 Chemical composition of individual locations (at.%)

Spectrum	Mg	Al	Cr	Mn	Zr
1	4.39	95.22	...	0.31	0.08
2	5.71	93.95	...	0.34	...
3	4.53	94.96	0.10	0.31	0.09
4	5.19	94.48	...	0.33	...
5	5.33	94.46	...	0.20	...
6	3.98	95.66	...	0.29	0.07
7	6.30	93.51	...	0.19	...
8	5.26	94.31	...	0.30	0.13
9	5.63	94.00	...	0.37	...

content > 3 wt.%) occurs by increasing the deposition speed. The higher the speed was set, the higher the magnesium content was documented. On the other hand, the higher the current used, the higher the losses were observed (Ref 49). The aluminum alloys are melted repeatedly as the heat source moves back and forth during WAAM process. Thus, the element loss of Mg in WAAM is like multi-pass welding but different from the single-pass welding (Ref 50). When the current increased, the loss of Mg was close to 1/5 of the Mg element content of the wire. When the deposition rate increased from 1.7 to 3.3 mm/s a loss rate of elemental Mg of about 5.5% (from 16.88 to 11.32%) was observed (Ref 51). Figure 24 shows the fracture area from which the magnesium content from Fig. 23(c) was evaluated.

A main role is played by the type of aluminum alloy and its susceptibility to porosity, which directly effects the mechanical properties. Higher strength of parallel overlay welding direction test specimens (approximately 6%) was achieved. The parallel tension generally resists grain boundary forces, whereas the perpendicular tension mainly resists the forces inside the grains and the bonding forces between deposited layers (Ref 52). In the specimens investigated in this study, the tensile strengths of parallel removed samples exceeded the tensile strengths of perpendicular removed samples. This finding indicates that the interlaminar combination was poorer and that the forces inside the grains exceeded the forces at the grain boundary. This indicates that the tensile strength between the grain boundaries exceeded that inside the grains derived from the growth direction between the grain boundaries (Ref 53). There was crack dissemination along the region of minimum energy consumption. Properties of samples produced by additive manufacturing are affected by anisotropy, the degree of anisotropy is characterized using the following equation (Ref 54):

$$A_p = \frac{P_{\max} - P_{\min}}{P_{\max}} \times 100\% \quad (\text{Eq 3})$$

where  $A_p$  is the anisotropic percentage,  $P_{\max}$  and  $P_{\min}$  represents the maximum and minimum strengths of the horizontal or vertical samples, respectively.

Also, it is necessary to consider the cohesion of the layers in the welding direction compared to the non-uniformity of the



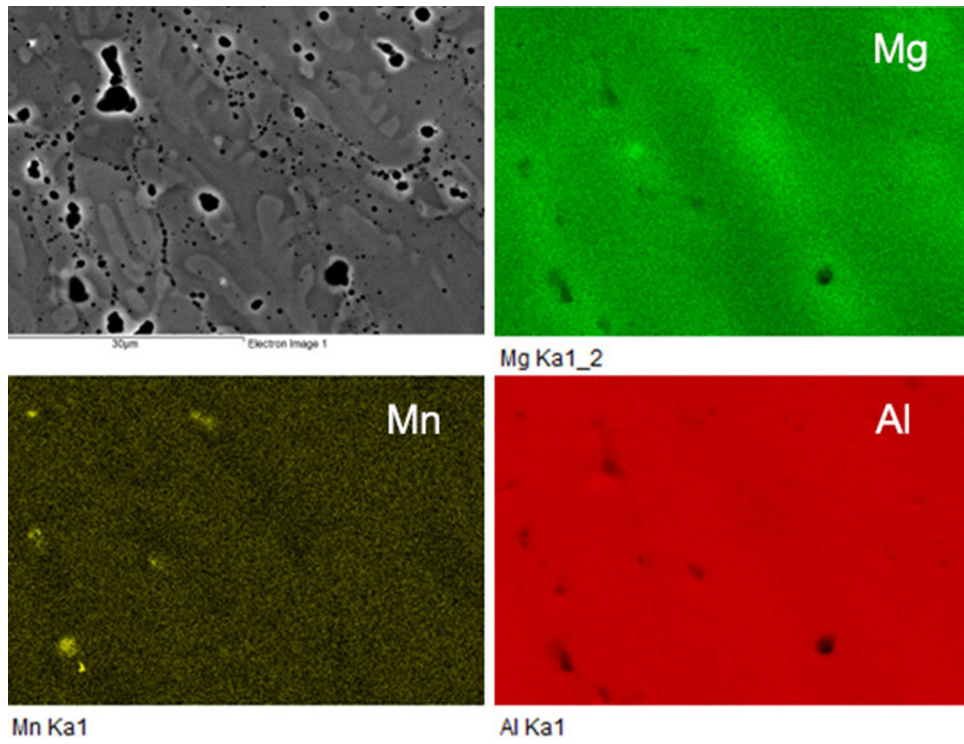


**Fig. 19** SEM-EDS elemental mapping of wall No. 1

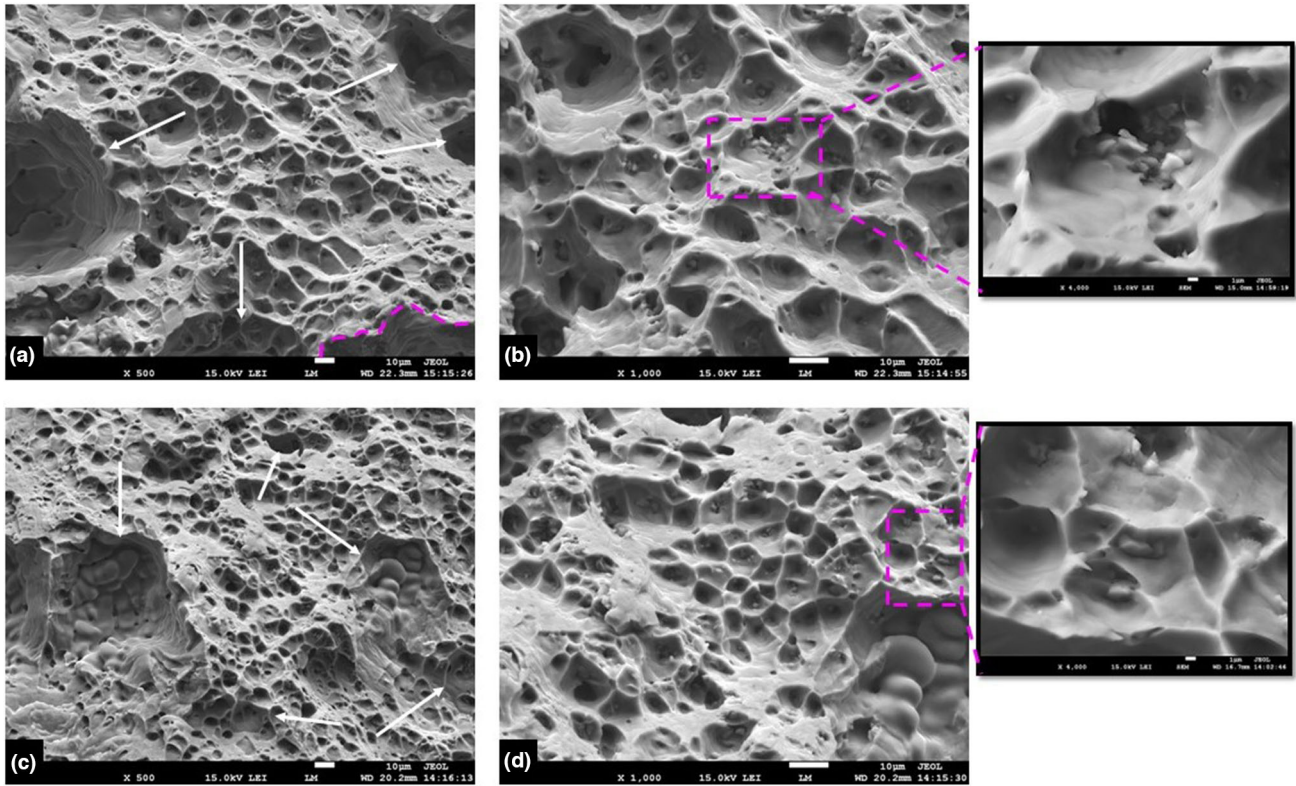


**Fig. 20** Fracture surfaces after tensile testing wall No. 1 (a, b) in perpendicular direction, (c, d) in parallel direction



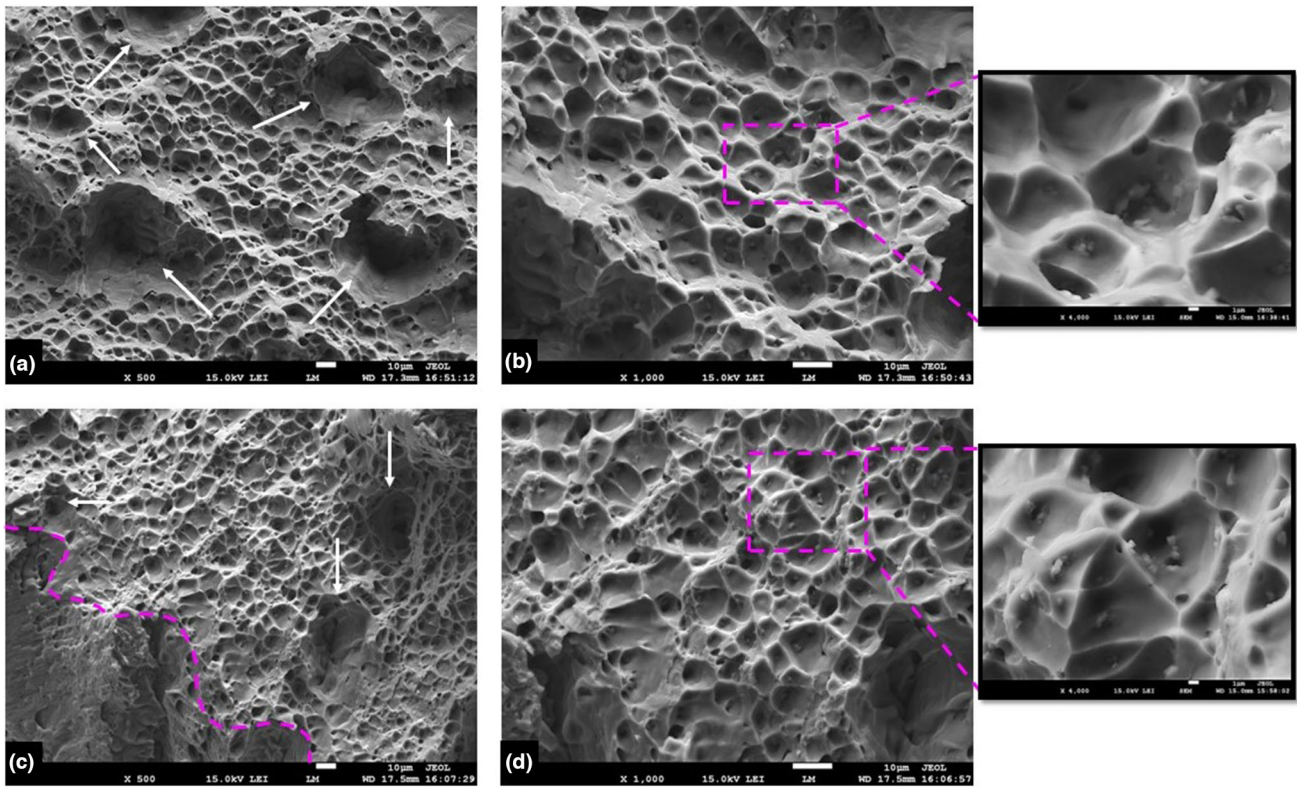


**Fig. 21** Fracture surfaces after tensile testing wall No. 2 (a, b) in perpendicular direction, (c, d) in parallel direction

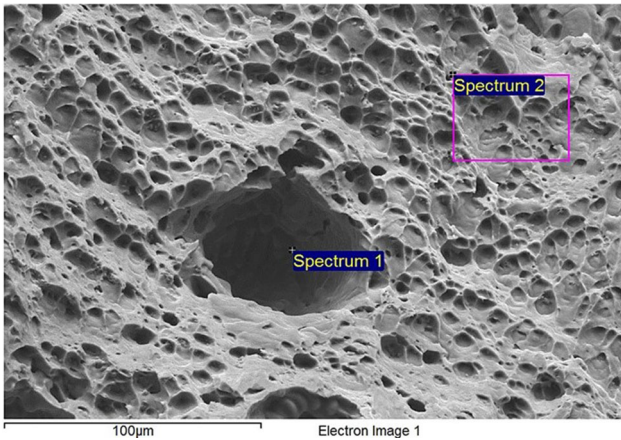


**Fig. 22** Locations of measurement of local chemical composition by means of EDS analysis (wall No. 1 parallel)

**Table 7** EDS point analysis in local sites (in at.%)

Spectrum	O	Mg	Al	Mn	Fe	Zr
Spectrum 1	6.18	7.15	81.31	2.98	2.38	...
Spectrum 2	2.86	5.66	90.89	0.39	0.09	0.11

layers in the perpendicular direction. To improve the cohesion of the layers in the perpendicular direction, resistance heat helps improve the melting of the wire and reduces the arc energy input, thereby removing hydrogen impurities on the surface of the individual layers and improve deposition efficiency (Fig. 25) (Ref 55). Klein et al. observed that difference in mechanical properties in perpendicular and parallel direction is dedicated to the location and concentration of the porosity. In the case of perpendicular samples, the crack propagation was due small distances between pores (Ref 56).

The welding parameters like welding current, voltage, wire feed speed (WFS) and travel speed (TS) have important effect on the porosity. The welding current and voltage were used the same, i.e., 85 A and 13.9 V. Thus, the influence of WFS and TS is evident. Ayarkwa analyzed in his study the influence of WFS/TS ratio on the porosity of weld metal. Higher ratio of WFS to TS resulted in higher amount of material to be deposited increasing the cross-section and size of the deposited weld bead. Larger molten metal area limits the escape velocity for the hydrogen from the molten pool which raises the porosity. This is in accordance with the research performed. Wall No. 1 deposited with the travel speed of 5 mm/s possesses the WFS/TS ratio equalling to about 17. The wall No. 2 which was deposited by TS of 7.5 mm/s was characterized by the WFS/TS of about 11. As it was mentioned above the cross-sectional area of the single bead deposited by the TS of 5 mm/s was 110 mm<sup>2</sup> and that produced with the TS of 7.5 mm/s was 140 mm<sup>2</sup> (Fig. 4). Higher WFS/TS ratio means the higher heat input that will increase the cooling time and enables more time to escape the hydrogen from the molten pool during solidification (Ref 57).

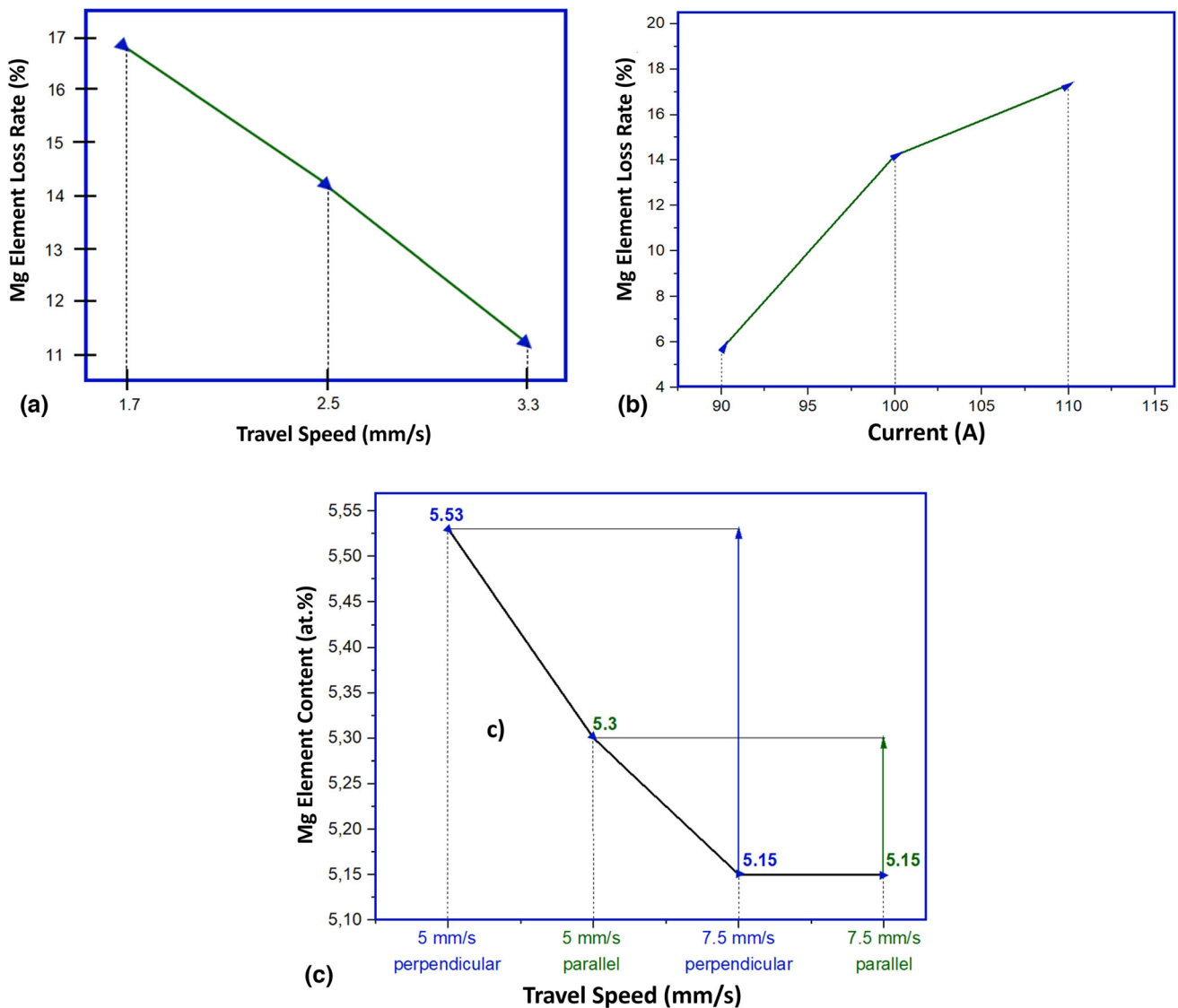


**Fig. 23** Influence of (a) travel speed and (b) welding current on Mg loss rate, according to Yuan et al. (Ref 50), (b) Mg elemental loss rate depending on current, according to Yuan et al. (Ref 50), (c) influence of travel speed on the Mg content according to this study

Higher strength at a higher travel speed, when the grains are finer, was expected. Since a concentration of porosity was found at the layer boundaries, the anisotropy between the vertical and horizontal directions can be attributed to the cross-sectional weakening by the pores, and crack initiation by stress concentration at the pores, and inhomogeneity of microstructures (Ref 58). Due to the occurrence of greater porosity, test specimen made at a lower welding speed achieved higher strength. Theories of the formation of pores at a higher travel speed were addressed by Fu et al. (Ref 59). The conditions of pores growth are expressed by equation:

$$P_h > 1 + 2\sigma_{2,g}/r \quad (\text{Eq 4})$$

where  $P_h$  is the pressure inside the pore,  $\sigma_{2,g}$  is the surface tension between the pore and the liquid, and  $r$  is the curvature radius (Ref 60).

When the arc energy is decreased, the melt temperature decreases and the cooling rate increases, so  $\sigma_{2,g}$  value was higher, and  $P_h$  was lower. At a higher travel speed (7.5 mm/s), less heat was supplied. The escape velocity decreased due to

the increase in liquid viscosity and the decrease in the radius of curvature, i.e., more pores were discovered (Fig. 16). The lower heat input limited the growth and separation of the pores, thus their ability to escape was limited (Ref 59).

## 5. Conclusion

The study presents analysis of the properties of 5087 aluminum alloy components produced by MIG-based WAAM technique. Two walls were made at different welding speeds (5 and 7.5 mm/s). The WAAMed components were analyzed by visual inspection, macroscopic and confocal microscopic analysis, EDS chemical composition analysis and mechanical properties testing. The influence of travel speed on the walls properties was evaluated. The work conclusions are as follows:

- Higher travel speed affected the wall width and overlay weld geometry. Increase in welding speed led to a narrowing of wall width from 10.23 to 8.44 mm,



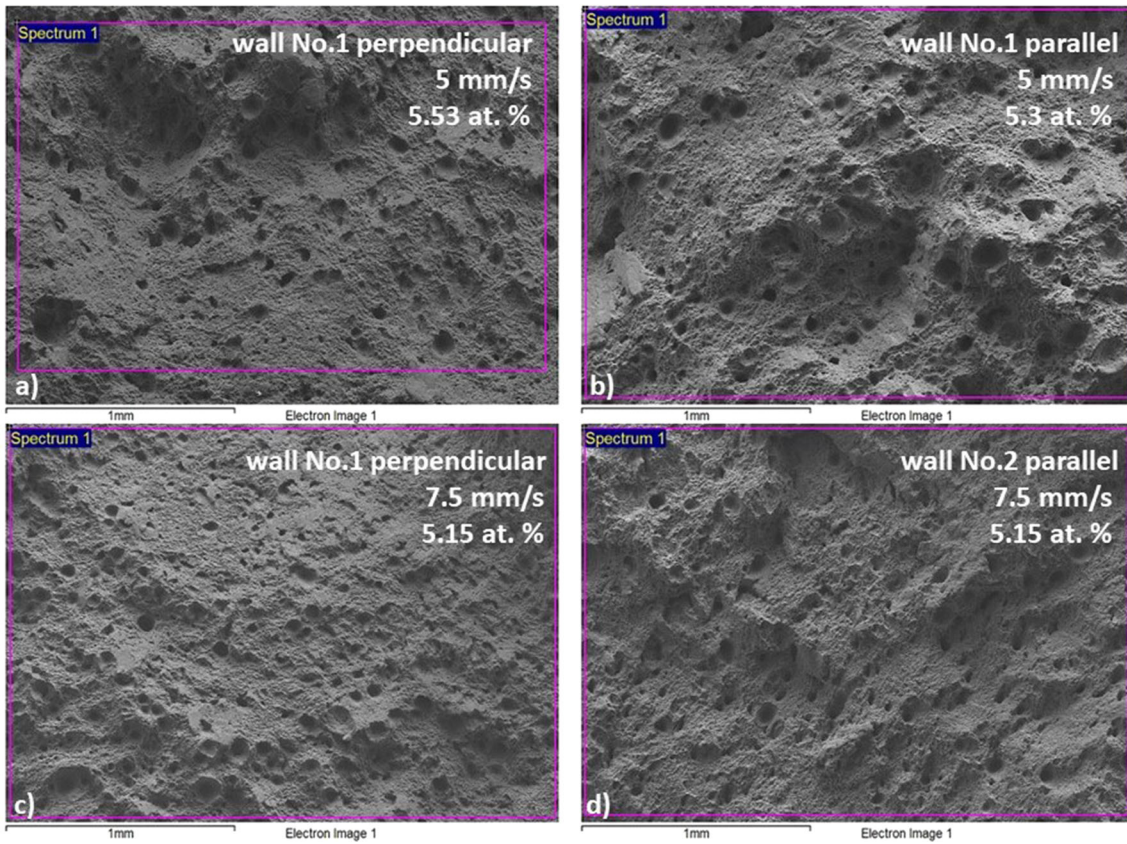


Fig. 24 Fracture areas from which the magnesium content was measured

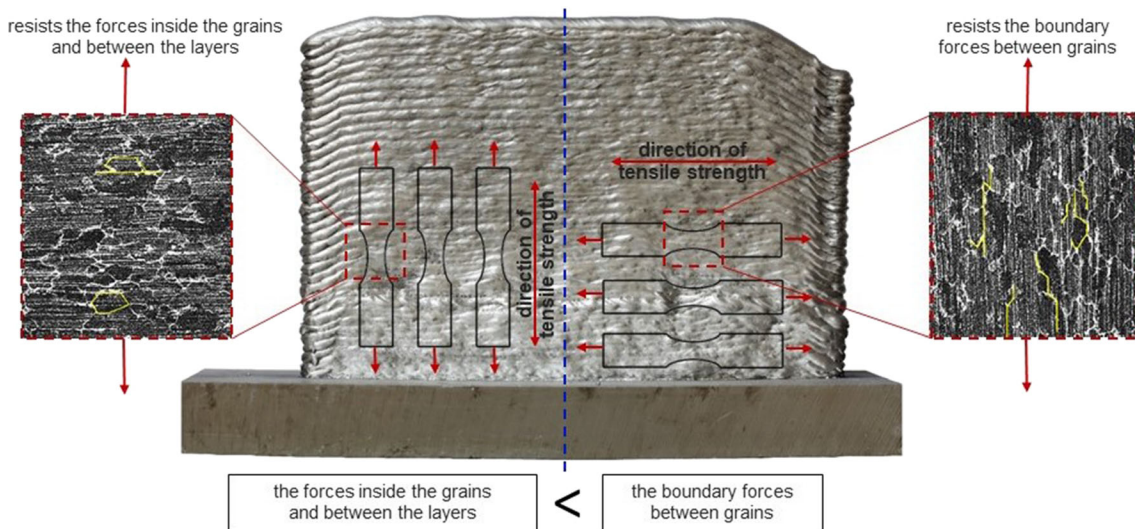


Fig. 25 Schematic representation of the forces within the grains (perpendicular and parallel direction) of the test specimens

- Higher travel speed caused the increase in the number of layers from 55 to 70 being necessary to manufacture the wall with the height of about 105 mm,
- Higher travel speed resulted in the decrease in tensile strength from 276 to 261 MPa (parallel samples) and from 262 to 246 MPa (perpendicular samples),
- Higher travel speed had almost no effect on the ductility of perpendicular samples and led to the increase in ductility from 16.96 to 17.32% of parallel samples,
- Higher travel caused increase in the porosity amount in weld metal. The porosity levels for different locations were 0.66% for weld metal produced with travel speed of 5 mm/s and 1.13% in the case of higher travel speed 7.5 mm/s.



## Acknowledgments

This work was supported by the VEGA grant agency of the Ministry of Education, Science, Research and Sport of the Slovak Republic, project No 1/0287/21 and No. 1/0796/20. The paper was prepared also with the support of the Ministry of Education, Youth, and Sports of the Czech Republic.

## Funding

Open access publishing supported by the National Technical Library in Prague.

## Open Access

This article is licensed under a Creative Commons Attribution 4.0 International License, which permits use, sharing, adaptation, distribution and reproduction in any medium or format, as long as you give appropriate credit to the original author(s) and the source, provide a link to the Creative Commons licence, and indicate if changes were made. The images or other third party material in this article are included in the article's Creative Commons licence, unless indicated otherwise in a credit line to the material. If material is not included in the article's Creative Commons licence and your intended use is not permitted by statutory regulation or exceeds the permitted use, you will need to obtain permission directly from the copyright holder. To view a copy of this licence, visit <http://creativecommons.org/licenses/by/4.0/>.

## References

1. B. Wu, Z. Pan, D. Ding, D. Cuiuri, H. Li, J. Xu, and J. Norrish, A Review of the Wire Arc Additive Manufacturing of Metals: Properties, Defects and Quality Improvement, *J. Manuf. Process.*, 2018, **35**, p 127–139. <https://doi.org/10.1016/j.jmapro.2018.08.001>
2. Y. Zhang, F. Cheng, and S. Wu, The Microstructure and Mechanical Properties of Duplex Stainless Steel Components Fabricated via Flux-Cored Wire Arc-Additive Manufacturing, *J. Manuf. Process.*, 2021, **69**, p 204–214. <https://doi.org/10.1016/j.jmapro.2021.07.045>
3. S. Liu and Y.C. Shin, Additive Manufacturing of Ti6Al4V Alloy: A Review, *Mater. Des.*, 2019, **164**, p 107552. <https://doi.org/10.1016/j.matdes.2018.107552>
4. N. Knezović, A. Topić, Wire and arc additive manufacturing (WAAM)—a new advance in manufacturing, in *Lecture Notes in Networks and Systems*, vol. 42 (Springer, 2019), pp. 65–71
5. J. Li, Y. Qiu, J. Yang, Y. Sheng, Y. Yi, X. Zeng, L. Chen, F. Yin, J. Su, T. Zhang et al., Effect of Grain Refinement Induced by Wire and Arc Additive Manufacture (WAAM) on the Corrosion Behaviors of AZ31 Magnesium Alloy in NaCl Solution, *J. Magnes. Alloys*, 2021 <https://doi.org/10.1016/j.jma.2021.04.007>
6. A. Horgar, H. Fostervoll, B. Nyhus, X. Ren, M. Eriksson, and O.M. Akselsen, Additive Manufacturing Using WAAM with AA5183 Wire, *J. Mater. Process. Technol.*, 2018, **259**, p 68–74. <https://doi.org/10.1016/j.jmatprotec.2018.04.014>
7. K. Wei, M. Gao, Z. Wang, and X. Zeng, Effect of Energy Input on Formability, Microstructure and Mechanical Properties of Selective Laser Melted AZ91D Magnesium Alloy, *Mater. Sci. Eng., A*, 2014, **611**, p 212–222. <https://doi.org/10.1016/j.msea.2014.05.092>
8. Z. Lin, K. Song, and X. Yu, A Review on Wire and Arc Additive Manufacturing of Titanium Alloy, *J. Manuf. Process.*, 2021, **70**, p 24–45. <https://doi.org/10.1016/j.jmapro.2021.08.018>
9. M.M. Tawfik, M.M. Nemat-Alla, and M.M. Dewidar, Enhancing the Properties of Aluminum Alloys Fabricated Using Wire + Arc Additive Manufacturing Technique - A Review, *J. Market. Res.*, 2021, **13**, p 754–768. <https://doi.org/10.1016/j.jmrt.2021.04.076>
10. W. Ou, T. Mukherjee, G.L. Knapp, Y. Wei, and T. DebRoy, Fusion Zone Geometries, Cooling Rates and Solidification Parameters during Wire Arc Additive Manufacturing, *Int. J. Heat Mass Transf.*, 2018, **127**, p 1084–1094. <https://doi.org/10.1016/j.ijheatmasstransfer.2018.08.111>
11. J.W. Elmer and G. Gibbs, The Effect of Atmosphere on the Composition of Wire Arc Additive Manufactured Metal Components, *Sci. Technol. Weld. Join.*, 2019, **24**, p 367–374. <https://doi.org/10.1080/13621718.2019.1605473>
12. C.G. Pickin and K. Young, Evaluation of Cold Metal Transfer (CMT) Process for Welding Aluminium Alloy, *Sci. Technol. Weld. Join.*, 2006, **11**, p 583–585. <https://doi.org/10.1179/174329306X120886>
13. H. Demir and S. Gündüz, The Effects of Aging on Machinability of 6061 Aluminium Alloy, *Mater. Des.*, 2009, **30**, p 1480–1483. <https://doi.org/10.1016/j.matdes.2008.08.007>
14. T.A. Rodrigues, V. Duarte, R.M. Miranda, T.G. Santos, and J.P. Oliveira, Current Status and Perspectives on Wire and Arc Additive Manufacturing (WAAM), *Materials*, 2019 <https://doi.org/10.3390/ma12071121>
15. B. Gungor, E. Kaluc, E. Taban, and S.I.K. Aydin, Mechanical and Microstructural Properties of Robotic Cold Metal Transfer (CMT) Welded 5083–H111 and 6082–T651 Aluminum Alloys, *Mater. Des.*, 2014, **54**, p 207–211. <https://doi.org/10.1016/j.matdes.2013.08.018>
16. T. Hauser, R.T. Reisch, S. Seebauer, A. Parasar, T. Kamps, R. Casati, J. Volpp, and A.F.H. Kaplan, Multi-Material Wire Arc Additive Manufacturing of Low and High Alloyed Aluminium Alloys with in-Situ Material Analysis, *J. Manuf. Process.*, 2021, **69**, p 378–390. <https://doi.org/10.1016/j.jmapro.2021.08.005>
17. Y. Zhou, X. Lin, N. Kang, W. Huang, J. Wang, and Z. Wang, Influence of Travel Speed on Microstructure and Mechanical Properties of Wire + Arc Additively Manufactured 2219 Aluminum Alloy, *J. Mater. Sci. Technol.*, 2020, **37**, p 143–153. <https://doi.org/10.1016/j.jmst.2019.06.016>
18. H. Mayer, M. Papakyriacou, B. Zettl, and S.E. Stanzl-Tschegg, Influence of Porosity on the Fatigue Limit of Die Cast Magnesium and Aluminium Alloys, *Int. J. Fatigue*, 2003, **25**, p 245–256. [https://doi.org/10.1016/S0142-1123\(02\)00054-3](https://doi.org/10.1016/S0142-1123(02)00054-3)
19. E.M. Ryan, T.J. Sabin, J.F. Watts, and M.J. Whiting, The Influence of Build Parameters and Wire Batch on Porosity of Wire and Arc Additive Manufactured Aluminium Alloy 2319, *J. Mater. Process. Technol.*, 2018, **262**, p 577–584. <https://doi.org/10.1016/j.jmatprotec.2018.07.030>
20. J.F. Rudy, E.J. Rupert, Effects of Porosity on Mechanical Properties of Aluminum Welds Increasing Area Fractions of Porosity in a Weld Cross Section Reduces Strength, and Fine Porosity-When Present in Sufficient Quantity to Contribute a Total Area Comparable to That of Large Pores-Effects a Loss in Strength as Much as Do Large Pores;
21. H. Toda, T. Hidaka, M. Kobayashi, K. Uesugi, A. Takeuchi, and K. Horikawa, Growth Behavior of Hydrogen Micropores in Aluminum Alloys during High-Temperature Exposure, *Acta Mater.*, 2009, **57**, p 2277–2290. <https://doi.org/10.1016/j.actamat.2009.01.026>
22. B. Zhang, C. Wang, Z. Wang, L. Zhang, and Q. Gao, Microstructure and Properties of Al Alloy ER5183 Deposited by Variable Polarity Cold Metal Transfer, *J. Mater. Process. Technol.*, 2019, **267**, p 167–176. <https://doi.org/10.1016/j.jmatprotec.2018.12.011>
23. T. Hauser, R.T. Reisch, P.P. Breese, Y. Nalam, K.S. Joshi, K. Bela, T. Kamps, J. Volpp, and A.F.H. Kaplan, Oxidation in Wire Arc Additive Manufacturing of Aluminium Alloys, *Addit. Manuf.*, 2021, **41**, p 101958. <https://doi.org/10.1016/j.addma.2021.101958>
24. A. Azarniya, A.K. Taheri, and K.K. Taheri, Recent Advances in Ageing of 7xxx Series Aluminum Alloys: A Physical Metallurgy Perspective, *J. Alloys Compd.*, 2019, **781**, p 945–983. <https://doi.org/10.1016/j.jallcom.2018.11.286>
25. S. Li, L.-J. Zhang, J. Ning, X. Wang, G.-F. Zhang, J.-X. Zhang, and S.-J. Na, Microstructures and Mechanical Properties of Al–Zn–Mg Aluminium Alloy Samples Produced by Wire+arc Additive Manufacturing, *J. Market. Res.*, 2020, **9**, p 13770–13780. <https://doi.org/10.1016/j.jmrt.2020.09.114>
26. J.Y. Bai, C.L. Fan, S.B. Lin, C.L. Yang, and B.L. Dong, Mechanical Properties and Fracture Behaviors of GTA-Additive Manufactured 2219-Al After an Especial Heat Treatment, *J. Mater. Eng. Perform.*, 2017, **26**, p 1808–1816. <https://doi.org/10.1007/s11665-017-2627-5>
27. S. Srivatsav, V. Jayakumar, and M. Sathishkumar, Recent Developments and Challenges Associated with Wire Arc Additive Manufac-

- turing of Al Alloy: A Review, *Mater. Today Proc.*, 2021, **46**, p 8561–8566. <https://doi.org/10.1016/j.matpr.2021.03.542>
28. J. Feng, H. Zhang, and P. He, The CMT Short-Circuiting Metal Transfer Process and Its Use in Thin Aluminium Sheets Welding, *Mater. Des.*, 2009, **30**, p 1850–1852. <https://doi.org/10.1016/j.matdes.2008.07.015>
  29. J.Y. Bai, C.L. Yang, S.B. Lin, B.L. Dong, and C.L. Fan, Mechanical Properties of 2219-Al Components Produced by Additive Manufacturing with TIG, *Int. J. Adv. Manuf. Technol.*, 2016, **86**, p 479–485. <https://doi.org/10.1007/s00170-015-8168-x>
  30. J. Gu, J. Ding, S.W. Williams, H. Gu, J. Bai, Y. Zhai, and P. Ma, The Strengthening Effect of Inter-Layer Cold Working and Post-Deposition Heat Treatment on the Additively Manufactured Al–6.3Cu Alloy, *Mater. Sci. Eng. A*, 2016, **651**, p 18–26. <https://doi.org/10.1016/j.msea.2015.10.101>
  31. Z. Qi, B. Qi, B. Cong, H. Sun, G. Zhao, and J. Ding, Microstructure and Mechanical Properties of Wire + Arc Additively Manufactured 2024 Aluminium Alloy Components: As-Deposited and Post Heat-Treated, *J. Manuf. Process.*, 2019, **40**, p 27–36. <https://doi.org/10.1016/j.jmapro.2019.03.003>
  32. C. Zhang, Y. Li, M. Gao, and X. Zeng, Wire Arc Additive Manufacturing of Al-6Mg Alloy Using Variable Polarity Cold Metal Transfer Arc as Power Source, *Mater. Sci. Eng. A*, 2018, **711**, p 415–423. <https://doi.org/10.1016/j.msea.2017.11.084>
  33. G. Yongfei, L. Weipeng, H. Zhiheng, Z. Chunxiang, and L. Junting, 5083 Aluminum Alloy Sheet with Excellent Mechanical Properties Fabricated by Constrained Ring Groove Pressing Based on a Cyclic Stress State, *J. Mater. Process. Technol.*, 2021, **295**, p 117174. <https://doi.org/10.1016/j.jmatprotec.2021.117174>
  34. J. Gu, J. Ding, S.W. Williams, H. Gu, P. Ma, and Y. Zhai, The Effect of Inter-Layer Cold Working and Post-Deposition Heat Treatment on Porosity in Additively Manufactured Aluminum Alloys, *J. Mater. Process. Technol.*, 2016, **230**, p 26–34. <https://doi.org/10.1016/j.jmatprotec.2015.11.006>
  35. J.K. Paik, Mechanical Properties of Friction Stir Welded Aluminum Alloys 5083 and 5383, *Naval Archit. Ocean Eng.*, 2009, **1**, p 39–49. <https://doi.org/10.3744/JNAOE.2009.1.1.039>
  36. J. Gu, X. Wang, J. Bai, J. Ding, S. Williams, Y. Zhai, and K. Liu, Deformation Microstructures and Strengthening Mechanisms for the Wire+arc Additively Manufactured Al-Mg4.5Mn Alloy with Inter-Layer Rolling, *Mater. Sci. Eng. A*, 2018, **712**, p 292–301. <https://doi.org/10.1016/j.msea.2017.11.113>
  37. S. Michna, J. Drápala, H. Schneider, A. Mišková, I. Lukáč, V. Očenášek, and R. Kořený Jaromír Drápala, Štefan Michna • Ivan Lukáč • Vladivoj Očenášek • Rudolf Kořený;
  38. A. Kumar, S.S. Gautam, and A. Kumar, Heat Input & Joint Efficiency of Three Welding Processes TIG, MIG and FSW using AA6061 (2014)
  39. A. Mishra, Friction Stir Welding of Dissimilar Metal: A Review, *SJ Impact Factor*, 2018, **6**, p 887. <https://doi.org/10.22214/ijraset.2018.13032>
  40. L. Liu, D. Ren, and F. Liu, A Review of Dissimilar Welding Techniques for Magnesium Alloys to Aluminum Alloys, *Materials*, 2014, **7**, p 3735–3757
  41. L. Ptáček, Nauka o Materiálu I Ptáček, *Akademické nakladatelství CERM*, 516 (2003)
  42. B. Mareš, ZÁKLADY STROJÁRSKEJ VÝROBY
  43. A.P. Boeira, L.L. Ferreira, and A. Garcia, Alloy Composition and Metal/Mold Heat Transfer Efficiency Affecting Inverse Segregation and Porosity of as-Cast Al-Cu Alloys, *Mater. Des.*, 2009, **30**, p 2090–2098. <https://doi.org/10.1016/j.matdes.2008.08.032>
  44. S. Singh, S.K. Sharma, and D.W. Rathod, A Review on Process Planning Strategies and Challenges of WAAM, *Mater. Today Proc.*, 2021, **47**, p 6564–6575. <https://doi.org/10.1016/j.matpr.2021.02.632>
  45. M. Arana, E. Ukar, I. Rodriguez, D. Aguilar, and P. Álvarez, Influence of Deposition Strategy and Heat Treatment on Mechanical Properties and Microstructure of 2319 Aluminium WAAM Components, *Mater. Des.*, 2022, **221**, p 110974. <https://doi.org/10.1016/j.matdes.2022.110974>
  46. A. Kumar Sinha, S. Pramanik, and K.P. Yagati, Research Progress in Arc Based Additive Manufacturing of Aluminium Alloys—A Review, *Measurement*, 2022, **200**, p 111672. <https://doi.org/10.1016/j.measurement.2022.111672>
  47. *Welding - Technical Information*
  48. L. Ren, H. Gu, W. Wang, S. Wang, C. Li, Z. Wang, Y. Zhai, and P. Ma, Effect of Mg Content on Microstructure and Properties of Al–Mg Alloy Produced by the Wire Arc Additive Manufacturing Method, *Materials*, 2019, **12**, p 4160. <https://doi.org/10.3390/ma12244160>
  49. R. Guan, D. Tie, Z. Li, Y. An, X. Wang, Q. Li, and X. Chen, Microstructure Evolution and Mechanical Property Improvement of Aluminum Alloys with High Magnesium Content during Continuous Rheo-Extrusion, *Mater. Sci. Eng., A*, 2018, **738**, p 31–37. <https://doi.org/10.1016/j.msea.2018.09.090>
  50. J.P. Oliveira, T.G. Santos, and R.M. Miranda, Revisiting Fundamental Welding Concepts to Improve Additive Manufacturing: From Theory to Practice, *Prog. Mater. Sci.*, 2020, **107**, p 100590. <https://doi.org/10.1016/j.pmatsci.2019.100590>
  51. T. Yuan, Z. Yu, S. Chen, M. Xu, and X. Jiang, Loss of Elemental Mg during Wire + Arc Additive Manufacturing of Al-Mg Alloy and Its Effect on Mechanical Properties, *J. Manuf. Process.*, 2020, **49**, p 456–462. <https://doi.org/10.1016/j.jmapro.2019.10.033>
  52. W. Wu, J. Xue, L. Wang, Z. Zhang, Y. Hu, and C. Dong, Forming Process, Microstructure, and Mechanical Properties of Thin-Walled 316L Stainless Steel Using Speed-Cold-Welding Additive Manufacturing, *Metals (Basel)*, 2019 <https://doi.org/10.3390/met9010109>
  53. T. Wang, Y. Zhang, Z. Wu, and C. Shi, Microstructure and Properties of Die Steel Fabricated by WAAM Using H13 Wire, *Vacuum*, 2018, **149**, p 185–189. <https://doi.org/10.1016/j.vacuum.2017.12.034>
  54. J. Alcisto, A. Enriquez, H. Garcia, S. Hinkson, T. Steelman, E. Silverman, P. Valdovino, H. Gigerenzer, J. Foyos, J. Ogren et al., Tensile Properties and Microstructures of Laser-Formed Ti-6Al-4V, *J. Mater. Eng. Perform.*, 2011, **20**, p 203–212. <https://doi.org/10.1007/s11665-010-9670-9>
  55. Z. Nie, G. Wang, J.D. McGuffin-Cawley, B. Narayanan, S. Zhang, D. Schwam, M. Kottman, and Y. Rong, Experimental Study and Modeling of H13 Steel Deposition Using Laser Hot-Wire Additive Manufacturing, *J. Mater. Process. Technol.*, 2016, **235**, p 171–186. <https://doi.org/10.1016/j.jmatprotec.2016.04.006>
  56. T. Klein, M. Schnall, B. Gomes, P. Warczok, D. Fleischhacker, and P.J. Morais, Wire-Arc Additive Manufacturing of a Novel High-Performance Al-Zn-Mg-Cu Alloy: Processing, Characterization and Feasibility Demonstration, *Addit. Manuf.*, 2021, **37**, p 101663. <https://doi.org/10.1016/j.addma.2020.101663>
  57. K. Ayarkwa, S. Williams, and J. Ding, Investigation of Pulse Advance Cold Metal Transfer on Aluminium Wire Arc Additive Manufacturing, *Int. J. Rapid Manuf.*, 2015 <https://doi.org/10.1504/IJRAPIDM.2015.073547>
  58. S.W. Williams, F. Martina, A.C. Addison, J. Ding, G. Pardal, and P. Colegrove, Wire + Arc Additive Manufacturing, *Mater. Sci. Technol.*, 2016, **32**, p 641–647. <https://doi.org/10.1179/1743284715Y.0000000073>
  59. R. Fu, S. Tang, J. Lu, Y. Cui, Z. Li, H. Zhang, T. Xu, Z. Chen, and C. Liu, Hot-Wire Arc Additive Manufacturing of Aluminum Alloy with Reduced Porosity and High Deposition Rate, *Mater. Des.*, 2021, **199**, p 109370. <https://doi.org/10.1016/j.matdes.2020.109370>
  60. M. Yang, Z. Yang, B. Cong, and B. Qi, How Ultra High Frequency of Pulsed Gas Tungsten Arc Welding Affects Weld Porosity of Ti-6Al-4V Alloy, *Int. J. Adv. Manuf. Technol.*, 2015, **76**, p 955–960. <https://doi.org/10.1007/s00170-014-6324-3>

**Publisher's Note** Springer Nature remains neutral with regard to jurisdictional claims in published maps and institutional affiliations.